

J. E. Hammer · K. V. Cashman · R. P. Hoblitt  
S. Newman

## Degassing and microlite crystallization during pre-climactic events of the 1991 eruption of Mt. Pinatubo, Philippines

Received: 4 December 1997 / Accepted: 13 September 1998

**Abstract** Dacite tephra produced by the 1991 pre-climactic eruptive sequence at Mt. Pinatubo display extreme heterogeneity in vesicularity, ranging in clast density from 700 to 2580 kg m<sup>-3</sup>. Observations of the 13 surge-producing blasts that preceded the climactic plinian event include radar-defined estimates of column heights and seismically defined eruptive and intra-eruptive durations. A comparison of the characteristics of erupted material, including microlite textures, chemical compositions, and H<sub>2</sub>O contents, with eruptive parameters suggests that devolatilization-induced crystallization of the magma occurred to a varying extent prior to at least nine of the explosive events. Although volatile loss progressed to the same approximate level in all of the clasts analyzed (weight percent H<sub>2</sub>O=1.26–1.73), microlite crystallization was extremely variable (0–22%). We infer that syn-eruptive volatile exsolution from magma in the conduit and intra-eruptive separation of the gas phase was facilitated by the development of permeability within magma residing in the conduit. Correlation of maximum microlite crystallinity with repose interval duration (28–262 min) suggests that crystallization occurred primarily intra-eruptively, in response to the reduction in dissolved H<sub>2</sub>O content that occurred during the preceding event. Detailed textural characterization, including determination of three-dimensional shapes and crystal size distributions (CSD), was conducted on a subset of clasts in order to

determine rates of crystal nucleation and growth using repose interval as the time available for crystallization. Shape and size analysis suggests that crystallization proceeded in response to lessening degrees of feldspar supersaturation as repose interval durations increased. We thus propose that during repose intervals, a plug of highly viscous magma formed due to the collapse of vesicular magma that had exsolved volatiles during the previous explosive event. If plug thickness grew proportionally to the square root of time, and if magma pressurization increased during the eruptive sequence, the frequency of eruptive pulses may have been modulated by degassing of magma within the conduit. Dense clasts in surge deposits probably represent plug material entrained by each subsequent explosive event.

**Key words** Volatiles · Degassing · Microlite textures · Crystal size distribution · Pulsatory subplinian eruptions

### Introduction

#### Background and motivation for study

The 1991 eruptive activity of Mt. Pinatubo volcano, Philippines, included initial dome growth, vertical eruptions, surge-producing eruptions, a 9-h plinian event, caldera collapse, and subsequent dome emplacement. The climactic eruption was preceded by 17 smaller explosive eruptions within a period of 50 h. The character and timing of these pre-climactic eruptions are well documented, and information about density and clast-type distributions from the resulting deposits is already known (Hoblitt et al. 1996). Paired with detailed textural analysis of erupted pyroclasts, such data provide an unusual opportunity to establish links between eruptive behavior and magmatic processes. We examined products of Mount Pinatubo's surge-producing events to compare pyroclast characteristics with eruptive parameters, such as repose intervals and eruption durations,

Editorial responsibility: W. Hildreth

J. E. Hammer (✉) · K. V. Cashman  
Department of Geological Sciences, University of Oregon,  
Eugene, OR 97403–1272, USA

R. P. Hoblitt  
U.S. Geological Survey, Cascades Volcano Observatory,  
5400 MacArthur Blvd., Vancouver, WA 98661, USA

S. Newman  
Division of Geological and Planetary Sciences, California  
Institute of Technology, Pasadena, CA 91125, USA

with the goal of assessing the extent of volatile loss and resultant groundmass crystallization associated with each eruptive pulse. To simplify the compositional complexity of the Pinatubo eruptive sequence, we isolated for study the dacite produced during the surge-producing eruptions. Here we present results of: (a) a compositional study to determine the relationship of pre-climactic to climactic material; (b) a study of dissolved H<sub>2</sub>O in glasses to assess the degree of devolatilization experienced by surge material; and (c) a textural analysis to examine relationships among microlite crystallinity, crystal nucleation and growth rates, clast vesicularity, and eruptive parameters.

#### Pre-climactic eruptive sequence: 7–15 June 1991

The 1991 eruptive sequence is characterized by an evolution in both the physical characteristics of the explosive events and in the chemical composition of erupted material. Pertinent features of the pre-climactic erup-

tive sequence as observed by Hoblitt et al. (1996) are summarized in Table 1. Following the dome growth of 7–12 June the observational record of explosive events includes measurements of column height, eruptive duration, and repose interval duration for the entire sequence, which consisted of four vertical eruptions producing high, relatively narrow eruption columns followed by 13 pyroclastic fountains that produced radial pyroclastic surges. Quiescent gas emission occurred during repose periods between explosive events. In general, successive explosive events decreased in intensity: plume heights of the first three vertical eruptions exceeded 24 km, whereas the later ash clouds produced by surge-producing events decreased progressively in height to ~8 km. The frequency of surge-producing events generally increased with time, so that repose intervals between events, nearly 3 h at the beginning of the sequence, decreased to less than 20 min just before the climactic event. In contrast, eruptive durations of 4–25 min for the surge-producing events varied independently of eruptive intensity or frequency.

**Table 1** 1991 Mt. Pinatubo eruption chronology (data from Hoblitt et al. 1996)

phase	date	repose since previous event <sup>1</sup> (min)	seismic duration (min)	event	plume ht (km)
I	3/15–5/31/91			earthquakes beginning March 15, phreatic explosions April 2, continuing emission of steam and ash, constant release of seismic energy	
II	6/1–6/7/91			escalating seismic release, less SO <sub>2</sub> , tilt, increase in ash, concentration of shallow earthquake hypocenters beneath summit	
III	6/7/91			gas and ash emission	8
	6/7–12/91			dome growth and ash	2–3
	6/12/91		31	increased tremor	
IV	6/12/91		2	explosion, pyroclastic currents	?
	6/12/91		36	1st vertical eruption	19
	6/12/91			weak tephra emission	3–4
	6/12/91		~ 50	Long period seismic swarm	
	6/12/91	805	14	2nd vertical eruption	>24
	6/13/91		~120	Long period seismic swarm	
	6/13/91	575	5	3rd vertical eruption	>24
	6/13/91		25h	Long period seismic swarm	
	6/14/91	263	3	4th vertical eruption	21
V	6/14/91		?	eruptive activity	15
	6/14/91	124	7	1st surge-forming eruption	
	6/14/91			low level eruption – tephra emission	
	6/14/91	210	5	2nd surge-forming eruption	≥24
	6/14/91		62	low level eruption	5
	6/14/91	262	3	3rd surge-forming eruption	21
	6/15/91	112	3–23	4th surge-forming eruption	?
	6/15/91	79–99	4	5th surge-forming eruption	?
	6/15/91	174	3	6th surge-forming eruption	12
	6/15/91		56	intense tremor	
	6/15/91	132	?	7th surge-forming eruption	12?
	6/15/91	?	4–14	8th surge-forming eruption (gap in seismic data)	15?
	6/15/91	36–46	4–13	9th surge-forming eruption	?
	6/15/91	28–37	9	10th surge-forming eruption	8
	6/15/91	15	10	11th surge-forming eruption	?
	6/15/91	20	4	12th surge-forming eruption	?
	6/15/91	19	13	13th surge-forming eruption	?
VI	6/15/91	14	540	climactic eruption, caldera collapse	34?

Data are summarized from Hoblitt et al. (1996).

<sup>1</sup> minimum repose times are used in text and calculations

The dominant composition of the erupted magma changed from andesite to dacite through the pre-climactic eruptive sequence. A hybrid andesite formed by mixing of basalt and crystal-rich dacite was the first magma to reach the surface as a dome. Petrographic descriptions of the basalt, dacite, and hybrid andesite are given by Pallister et al. (1996) and Bernard et al. (1996). Andesite of the same composition was also ejected as scoria during the first several vertical eruptions. Meanwhile, beginning with the first vertical eruption, dacite made up an increasing fraction of erupted material, so that more than half (by clast frequency) of the material erupted by the third surge-producing blast was dacite (Hoblitt et al. 1996). The climactic event produced solely dacite magma (Pallister et al. 1996). The densities of dacite clasts generated by surge-producing events varies considerably, from 700 to 2580 kg m<sup>-3</sup>. In contrast, the climactic dacite was more uniformly vesicular, encompassing a density range of 700–1100 kg m<sup>-3</sup> (Hoblitt et al. 1996). The climactic dacite includes two texturally distinct types, referred to as phenocryst-rich and phenocryst-poor components (Pallister et al. 1996). The groundmass of phenocryst-poor material contains abundant phenocryst fragments, 1- to 2- $\mu$ m microlites, and spherical vesicles (Hammer and Cashman 1995). The groundmass of the phenocryst-rich component is microlite free and vesicles are large and elongate.

Surge deposits were extensively scoured away by pyroclastic flows generated during the climactic phase of the eruption. Although 13 surge-producing events are inferred from the seismic record (Hoblitt et al. 1996), the most surge units distinguished in an individual outcrop was 11. This precludes absolute correlation of an eruptive pulse with bed unit, although the later small surges are more likely than earlier events to be unrepresented in the deposit.

### Volatile loss and crystallization

The style, timing, and extent of sub-surface magma devolatilization may control eruptive parameters. Recent investigations of rhyolitic (Obsidian Dome, CA), rhyodacitic (Quizapu, Chile), andesitic (Santorini, Greece), and phono-tephritic (Vesuvius, Italy, 1906) systems demonstrate that juvenile, petrologically indistinguishable magmas may erupt as explosive tephra or effusive lava, depending on the manner and extent of subsurface degassing (Eichelberger et al. 1986; Hildreth and Drake 1992; Mastrolorenzo et al. 1993; Mellors and Sparks 1991). Because hydrogen isotopes are fractionated during volatile loss, isotopic analysis of dissolved H<sub>2</sub>O yields information about the systematics of this process. Isotopic studies of the Mono Craters tephra (Bursik 1993; Newman et al. 1988), Mount St. Helens blast dacite (Hoblitt and Harmon 1993), and Quizapu dacite (Hildreth and Drake 1992) show that effusive eruptions are dominated by open-system degassing. Conversely,

isotopic signatures related to closed-system fractionation characterize explosively erupted tephra and indicate that gas is not physically separated from the magma prior to fragmentation. Magma ascent rate may determine the style of degassing, with a slow rate of ascent facilitating permeability development in the vesiculating magma and resulting in open-system conditions (Eichelberger et al. 1986; Klug and Cashman 1996). Additionally, permeability may be increased syn-eruptively through bubble elongation resulting from shear at the conduit walls (Cashman and Mangan 1994). In either case, bubble collapse following (and aided by) elongation and permeability development may result in clasts that are consequently denser (up to 2600 kg m<sup>-3</sup>) than typical pumice (600–900 kg m<sup>-3</sup>). External pressure is another factor that may influence the style (open vs closed) of degassing, and may be reflected in the total H<sub>2</sub>O content of erupted glasses (Newman et al. 1988). Calculated pressures range from atmospheric (0.1 wt.% H<sub>2</sub>O; Westrich et al. 1988) to lithostatic at a depth of  $\approx$  2 km (Bursik 1993), indicating that degassing may occur over a wide range of pressures (depths) to the extent allowed by ascent rate and magma and host-rock permeabilities.

Devolatilization of a rhyolite liquid from 3–5 wt.% to 0.1–1 wt.% H<sub>2</sub>O can result in an effective undercooling up to 200 °C (Swanson 1977), triggering crystallization of the liquid (Eichelberger et al. 1986). Although devolatilization-induced crystallization has been inferred for several volcanic systems (Cashman 1992; Nakada and Motomura 1995; Swanson et al. 1989), experimental verification that it can occur over eruptive time scales in silicic magmas has only been obtained for Mount St. Helens dacite (Geschwind and Rutherford 1995), where plagioclase microlites grew in response to rapid isothermal decompression of an H<sub>2</sub>O-saturated dacite (having a rhyolite liquid) from 160 to 2 MPa. Isothermal decompression-induced crystallization has been inferred in natural systems where rates of supersaturations driving crystallization are substantially greater than cooling rates (Swanson et al. 1989; Gardner et al. 1998; Hammer et al., in press).

Dense, degassed pyroclasts have been interpreted as material from the conduit lining (Bursik 1993; Wolf and Eichelberger 1997), quenched lava lakes (Mellors and Sparks 1991), and shallow intrusive domes (Hoblitt and Harmon 1993) entrained during the fragmentation of gas-rich magmatic or hydrovolcanic eruptions. In these cases the degassed material may be used to infer eruptive parameters such as fragmentation depth and eruption intensity. These investigations show that significant degassing and subsequent vesicle collapse occur over eruptive time scales, and they underscore the value of examining poorly vesicular material produced during explosive eruptions in the study of eruption mechanisms. However, the possibility that degassing may play a role in *determining* eruption dynamics has been largely unexplored. As viscosity increases dramatically through both devolatilization of the liquid and the pro-

duction of new crystals, the rheological effects of these processes may have a significant effect on the subsequent course of eruptive events.

## Methods

### Samples

Most of the clasts analyzed here were collected in March 1992 approximately 4 km southeast of the pre-climactic lava dome (site #11; Hoblitt et al. 1996). Surge beds from 11 eruptions were identified at this site. Nine of these, surge 1 and surges 3–10, yielded sufficient material for analysis. Because 13 surges were observed on

14–15 June 1991, but deposits from only 11 were identified at this site, the bed assignment numbers may differ from the actual sequence numbers. Because less material was preserved from the later events, uncertainty is probably greatest for surges 8–13. However, since the later events shared similar intensities and repose interval durations, uncertainty in bed-event assignment does not significantly affect the results of this study. Between two and 12 of the denser clasts from each of the nine surge units were selected for study. Clast names and densities are listed by surge event in Table 2. Also analyzed were one andesite clast from the pre-climactic dome, two andesite clasts from the first vertical eruption, and two dacite clasts from the climactic eruption (all courtesy of J. Pallister).

**Table 2** Clast densities and textural characterizations

surge event <sup>1</sup>	sample	clast density (g cm <sup>-3</sup> )	no. images	reference area (μm <sup>2</sup> )	number of microlites counted	microlite volume fraction, $\phi$	avg. microlite size, $s_n$ (μm)	microlite area number density, $N_A$ (mm <sup>-2</sup> )
1	P101 <sup>2</sup>	2.38	6	14461	1269	0.075 (0.028)	0.90 (0.20)	87754 (21649)
1	P111	2.38	4	10077	1342	0.061 (0.009)	0.68 (0.02)	133178 (20293)
1	P121	2.19	5	11084	717	0.075 (0.008)	1.07 (0.06)	64686 (6673)
3	P301 <sup>3</sup>	2.47	5	11449	1404	0.157 (0.036)	1.13 (0.08)	122628 (34318)
3	P311 <sup>2,3</sup>	2.42	7	16061	762	0.134 (0.024)	1.67 (0.19)	47445 (5386)
3	P302	1.72	6	12240	346	0.017 (0.006)	0.78 (0.08)	28268 (9086)
3	P331	1.96	5	8319	172	0.072 (0.052)	1.80 (0.53)	20675 (10964)
3	P303	2.13	10	19211	2857	0.082 (0.011)	0.74 (0.10)	148718 (32976)
3	P051	n.d.	5	8491	871	0.057 (0.038)	0.89 (0.03)	102577 (27293)
3	P053	n.d.	5	7722	686	0.051 (0.008)	0.75 (0.08)	88839 (14103)
3	P321 <sup>3</sup>	2.06	4	9399	345	0.038 (0.007)	1.02 (0.03)	36707 (5955)
3	P312 <sup>2</sup>	2.32	4	8791	1673	0.121 (0.022)	0.80 (0.02)	190317 (32073)
3	P313	2.30	4	9248	981	0.073 (0.011)	0.83 (0.01)	106083 (19159)
3	P351	0.70	4	2962	66	0.011 (0.003)	0.70 (0.10)	22282 (1637)
3	P352	1.20	4	4319	32	0.004 (0.002)	0.77 (0.07)	7409 (3131)
4	P401 <sup>3</sup>	2.47	6	13881	2010	0.082 (0.021)	0.75 (0.07)	144800 (25696)
4	P411	2.48	4	7882	400	0.095 (0.007)	1.37 (0.04)	50749 (5217)
4	P412 <sup>3</sup>	2.49	5	10572	1188	0.145 (0.016)	1.13 (0.06)	112370 (20178)
4	P421 <sup>3</sup>	1.99	4	7660	862	0.097 (0.009)	0.93 (0.04)	112527 (8042)
4	P422	2.20	4	9146	950	0.093 (0.010)	0.95 (0.03)	103871 (10234)
4	P402	1.86	7	9545	1452	0.095 (0.010)	0.79 (0.05)	152123 (13368)
5	P501 <sup>3</sup>	2.38	11	21045	3046	0.106 (0.019)	0.85 (0.05)	144738 (16366)
5	P511 <sup>2,3</sup>	2.26	4	9554	580	0.051 (0.009)	0.92 (0.07)	60706 (14552)
6	P601	2.50	3	7124	480	0.035 (0.003)	0.72 (0.03)	67377 (5418)
6	P611 <sup>3</sup>	2.47	4	9872	168	0.013 (0.007)	0.86 (0.10)	17017 (5403)
6	P612	2.49	6	13859	1654	0.117 (0.037)	0.98 (0.14)	119343 (5273)
6	P613 <sup>2,3</sup>	2.58	6	13558	1245	0.218 (0.053)	1.53 (0.19)	91828 (5370)
6	P641	2.45	4	10233	178	0.011 (0.001)	0.81 (0.06)	17395 (3631)
6	P651	1.03	3	3777	73	0.012 (0.003)	0.78 (0.07)	19328 (3421)
7	P701 <sup>2</sup>	2.34	10	23376	2909	0.091 (0.027)	0.85 (0.09)	124442 (30917)
7	P711	2.32	4	10084	101	0.006 (0.002)	0.79 (0.05)	10016 (1969)
7	P702	1.38	7	10613	350	0.017 (0.004)	0.71 (0.08)	32978 (8305)
8	P101	n.d.	4	8245	161	0.013 (0.003)	0.82 (0.07)	19526 (5017)
8	P103	n.d.	8	14512	1285	0.053 (0.009)	0.77 (0.03)	88547 (14703)
8	P801	2.37	4	9841	16	0.001 (0.000)	0.80 (0.07)	1626 (486)
9	P901 <sup>2,3</sup>	2.29	7	17014	412	0.011 (0.004)	0.65 (0.14)	24216 (13671)
9	P911	1.97	6	12718	70	0.004 (0.001)	0.83 (0.10)	5504 (2567)
9	P902	1.32	4	6988	12	0.000 (0.000)	0.49 (0.26)	1732 (750)
9	P903	1.72	4	7785	42	0.002 (0.001)	0.65 (0.14)	5395 (490)
9	P951	0.83	4	2374	2	0.001 (0.001)	0.91 (0.64)	842 (869)
10	PE01	2.12	6	13523	28	0.001 (0.001)	0.75 (0.32)	2145 (1053)
10	PE02	1.57	4	7664	27	0.002 (0.001)	0.75 (0.03)	3523 (1136)

n.d. = not determined. ( ) =  $1\sigma$  of average

<sup>1</sup> Correlation of eruptive sequence with surge beds is a best-estimate (see text)

<sup>2</sup> selected for shape and CSD analysis

<sup>3</sup> selected for H<sub>2</sub>O analysis

Clast densities were obtained using Archimedes' principle following the method of Hoblitt and Harmon (1993). Clast density was converted to bulk vesicularity using two estimates of the vesicle-free (DRE) density. The first estimate,  $2740 \text{ kg m}^{-3}$ , is the calculated density given the compositional mode of a typical clast. The second estimate,  $2580 \text{ kg m}^{-3}$ , is the highest measured density for any single clast. Vesicularities calculated using the two estimates differ by an average of 5%. For our purposes, low-density tephra are defined as those with densities  $\leq 1800 \text{ kg m}^{-3}$ ; high-density, or simply dense, tephra are denoted by bulk densities  $\geq 1800 \text{ kg m}^{-3}$ . The high-density clasts are gray to black, and have either a vitreous or matte luster. Since the primary control on clast density is variation in vesicularity, rather than phenocryst content or composition, the terms clast density and bulk vesicularity are interchangeable. For the remainder of this paper, clast density is used since this is the parameter that was measured directly.

### Compositional analysis

Glass and feldspar microlite compositions were obtained from polished thin sections of Pinatubo andesite and dacite using a Cameca SX-50 electron microprobe at the University of Oregon utilizing a ZAF X-ray intensity reduction routine. Operating conditions for the analysis of feldspar included a 10 nA beam current and accelerating voltage of 15 keV. Plagioclase microlites ranging in length from 3 to 20  $\mu\text{m}$  were analyzed using the largest appropriate spot size. Glass compositions were obtained using a two-step analysis procedure described in Appendix A.

### H<sub>2</sub>O analysis

Total H<sub>2</sub>O (H<sub>2</sub>O<sub>T</sub>) contents were obtained using Fourier Transform Infrared (FTIR) spectroscopy. Analyses

were carried out at the California Institute of Technology using a NicPlan IR microscope connected to a Nicolet 60SX IR spectrophotometer. Spectra were obtained using 1024–2048 scans (with 114×114- and 69×69- $\mu\text{m}$  apertures, respectively), a liquid-nitrogen-cooled MCT detector and KBr beamsplitter. Four to nine spots were analyzed on each doubly polished slab, and repeat analyses were made at many spots to ensure reproducibility. Sample thicknesses (30–90  $\mu\text{m}$ ) were measured using a Mitutoyo digital gauge, accurate to within  $\pm 2 \mu\text{m}$ . The absorbance of given bands was used to determine the concentration of dissolved H<sub>2</sub>O species according to Eq.(1) from Newman et al. (1986):

$$c = (\text{MW}_{\text{H}_2\text{O}})(\text{abs})/[(\rho)(d)(\epsilon)], \quad (1)$$

where  $c$  is the concentration in weight fraction,  $\text{MW}_{\text{H}_2\text{O}}$  is the molecular weight of H<sub>2</sub>O ( $\text{g mol}^{-1}$ ),  $\rho$  is the density of the glass (values ranged from 2327 to 2344  $\text{g L}^{-1}$  using the method of Lange and Carmichael (1990) for silicate liquids where  $T = 780^\circ\text{C}$  and  $P = 100 \text{ bar}$ ),  $d$  is slab thickness (centimeters),  $\epsilon$  is molar absorptivity ( $\text{L mol}^{-1} \text{ cm}^{-1}$ ), and  $\text{abs}$  is absorbance (dimensionless). The high microlite content of many clasts precluded analysis of clear glass. However, since the microlite phases are anhydrous, their primary effect was to reduce the effective interaction volume within the sample. To account for the presence of microlites, measured slab thicknesses were adjusted according to:

$$d_{\text{adj}} = (d)(1 - \phi), \quad (2)$$

where  $d_{\text{adj}}$  is the corrected thickness and  $\phi$  is the volume fraction of microlites in the groundmass determined by image analysis (see Appendix C). Absorptivities for bands at 5200  $\text{cm}^{-1}$  (molecular H<sub>2</sub>O) and 4500  $\text{cm}^{-1}$  (OH<sup>-</sup> groups) were 1.61 and 1.73, respectively, following Newman et al. (1986). All H<sub>2</sub>O<sub>T</sub> values reported in Table 3 represent the sum of values obtained from the 5200 and 4500  $\text{cm}^{-1}$  bands except the most crystalline clast, P613, where the total H<sub>2</sub>O band (3550  $\text{cm}^{-1}$ ) was used with an absorption coefficient of

**Table 3** Average H<sub>2</sub>O<sub>T</sub> and speciation data (from FTIR) in Pinatubo dacite matrix glasses

sample	n	wt. % molecular H <sub>2</sub> O	wt. % OH- groups	H <sub>2</sub> O <sub>T</sub> <sup>1</sup> (wt. %)	max <sup>2</sup> (wt. %)	min <sup>3</sup> (wt. %)
P301	8	0.68	0.80	1.49 (0.41)	2.08	0.77
P311	10	0.48	0.83	1.31 (0.23)	1.62	0.91
P321	12	0.77	0.95	1.73 (0.32)	2.49	1.15
P401	5	0.53	0.78	1.31 (0.40)	2.01	1.02
P412	9	0.70	0.79	1.49 (0.22)	1.87	1.28
P421	5	0.70	0.94	1.64 (0.40)	2.06	1.00
P501	6	0.49	0.95	1.43 (0.06)	1.53	1.38
P511	10	0.67	0.92	1.59 (0.23)	2.04	1.14
P611	5	0.51	0.85	1.37 (0.12)	1.49	1.21
P613	5	n.d.	n.d.	1.26 (0.06)	1.34	1.20
P901	10	0.54	0.78	1.31 (0.12)	1.52	1.06

values are sample averages. ( ) =  $1\sigma$ . n.d. = not determined

<sup>1</sup> Sum of OH- and molecular H<sub>2</sub>O (except P613 – see text)

<sup>2</sup> maximum H<sub>2</sub>O<sub>T</sub> in sample

<sup>3</sup> minimum H<sub>2</sub>O<sub>T</sub> in sample

76 (computed using speciation data from the other clasts and Eq. (3) from Newman et al. 1986 with  $\epsilon_{\text{H}_2\text{O}, 3550} = 56 \text{ L mol}^{-1} \text{ cm}^{-1}$  and  $\epsilon_{\text{OH}, 3550} = 88 \text{ L mol}^{-1} \text{ cm}^{-1}$  from Newman et al. 1986 and Dobson et al. 1989). Externally derived  $\text{H}_2\text{O}$  can be incorporated into glass either before or after deposition. Appendix B includes an assessment of post-eruptive glass hydration.

### Textural analysis

High-magnification images from each clast were obtained using a JEOL 6300 SEM with a  $\text{LaB}_6$  gun operating at 10 keV and 15 mm working distance. All images used for quantitative measurements were taken at  $2000\times$  magnification to avoid problems of scale-dependent resolution. Textural analysis was carried out at two levels of detail. Following the characterization of microlite number density, crystallinity, and average crystal size for all of the clasts, a subset of seven clasts was selected for analysis of shape and crystal size distribution. For the initial characterization, 221 images from the 42 clasts were processed. A minimum of four images was deemed sufficient to characterize a relatively homogeneous clast. Heterogeneity in microlite size and spatial distribution was observed in several clasts. Correspondingly greater numbers of images were collected from these clasts with the goal of characterizing both the textural extremes and representative areas. For the detailed analysis, crystal size distributions (CSDs) and average shapes were obtained using between 223 and 483 crystals from each clast. All measurements were made using the image processing programs NIH Image and Prism View.

The most abundant phase, feldspar, was used to characterize groundmass textures in the Pinatubo dacite. Microlites were distinguished from microphenocrysts and broken phenocrysts by their euhedral habit and small size ( $<15 \mu\text{m}$  in the longest direction). Because only groundmass textures were examined, all terms describing crystal textures refer to microlites alone. Therefore, "crystallinity,"  $\phi$ , refers to the volume fraction of *feldspar microlites* in the groundmass only. Detailed descriptions of image processing methods, characterization of crystal textures, and CSD analysis are presented in Appendix C.

### Results

A range of vesicularities, groundmass textures, and compositions are represented in the 1991 eruptive products of Mount Pinatubo (Fig. 1). Magma produced during pre-climactic activity included dense microlite-charged andesite, erupted as a dome (Fig. 1a), scoriaeous microlite-free tephra from the first vertical eruption (Fig. 1b), and dacite that exhibited a range of crys-

tal textures (Fig. 1c–e). The climactic dacite was texturally distinguished as phenocryst-poor (Fig. 1f) and phenocryst-rich (Fig. 1g) varieties that were uniformly vesicular but differed in microlite content. Glass compositional analyses were obtained to distinguish between andesite scoria and dacite tephra (including pumice and cognate lithics) from the surge-producing events. Microlite-free, phenocryst-rich glass from the climactic pumice provided a basis for comparison among pre-climactic dacites of different microlite contents.

### Compositional analyses

#### Andesite glass

Glasses from three andesite samples representing dome lava, dense juvenile tephra, and scoria from the first vertical eruption are rhyolitic in composition and range from 77.1 wt.%  $\text{SiO}_2$  (dome) to 70.9 wt.%  $\text{SiO}_2$  (scoria; Table 4). The groundmass of the dome sample has a microlite content of  $\approx 25\%$ , whereas the scoria is microlite free, consistent with the measured variation in glass composition. A dense tephra clast from the first vertical eruption is similar to the dome in glass composition (76.9 wt.%  $\text{SiO}_2$ ), as well as microlite content ( $\sim 25\%$ ), but differs in that it is  $\sim 20\%$  vesicular while the dome is non-vesicular. Although variable extents of crystallization in the andesite and dacite magmas resulted in rhyolitic glass compositions for both, the glasses of the andesite can be identified by lower  $\text{Al}_2\text{O}_3$  and  $\text{Na}_2\text{O}$ , and higher  $\text{FeO}$ ,  $\text{TiO}_2$ , and  $\text{MgO}$  for a given  $\text{SiO}_2$  content (compare Tables 4 and 5). Neither of two clasts from the eighth surge-producing eruption originally thought to be andesite had glass compositions distinguishable from dacite glass, illustrating the difficulty in characterization of magma type based on physical appearance (especially color) alone.

**Table 4** Average matrix glass compositions of Pinatubo andesite

sample event	P001 dome	P031 (dense) 1st vertical	P011 (scoria) 1st vertical
n	7	5	7
$\text{SiO}_2$	77.4 (0.4)	76.9 (0.6)	70.9 (1.4)
$\text{TiO}_2$	0.53 (0.10)	0.37 (0.07)	0.35 (0.07)
$\text{Al}_2\text{O}_3$	11.1 (0.3)	12.0 (0.1)	14.9 (0.7)
$\text{MgO}$	0.33 (0.30)	0.20 (0.11)	0.78 (0.15)
$\text{CaO}$	0.85 (0.23)	0.80 (0.09)	2.52 (0.39)
$\text{MnO}$	0.03 (0.02)	0.05 (0.02)	0.07 (0.04)
$\text{FeO}_T$	1.48 (0.29)	1.53 (0.10)	2.58 (0.41)
$\text{Na}_2\text{O}$	2.62 (0.24)	2.94 (0.16)	2.19 (0.95)
$\text{K}_2\text{O}$	3.75 (0.48)	4.09 (0.09)	2.95 (0.17)
Cl	0.10 (0.04)	n.a.	n.a.
total	98.1 (0.5)	98.9 (0.5)	97.3 (1.0)

( ) = one standard deviation. n.a. = not analyzed

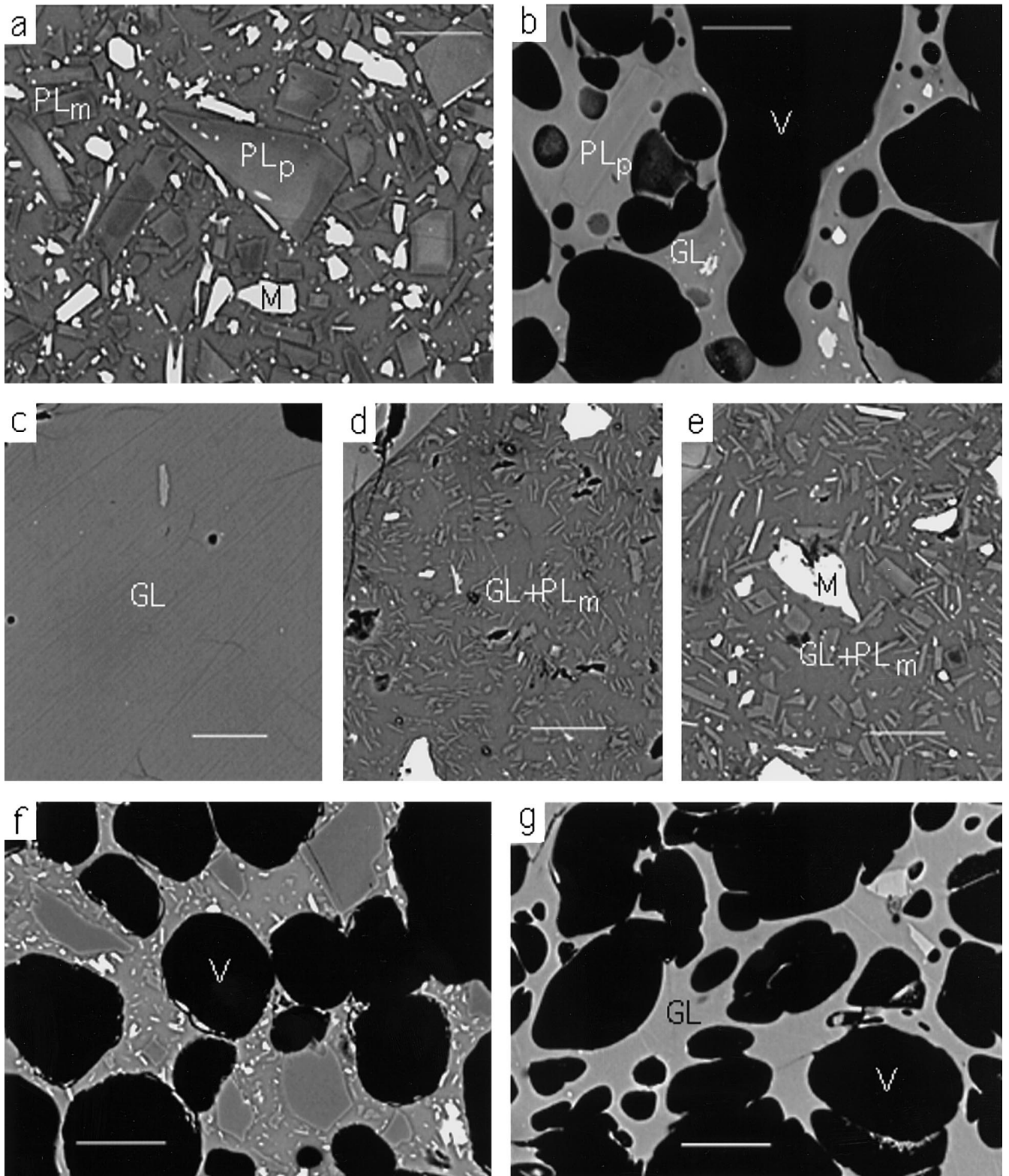


**Fig. 1a–g** Backscattered electron (BSE) images of 1991 Pinatubo eruptive products. All scale bars are 10  $\mu\text{m}$ .  $\text{PL}_p$  plagioclase phenocryst (whole or fragment thereof);  $\text{PL}_m$  plagioclase microlite; GL glass; V vesicle; M mafic mineral. **a** Crystalline andesite

dome. **b** Vesicular andesite scoria from the first vertical eruption. **c, d, e** Pre-climactic dacite. **f** Phenocryst-poor climactic dacite. **g** phenocryst-rich climactic dacite (no phenocrysts appear in this image)

## Dacite glass

Glass compositions of dense and vesicular dacite clasts having similar microlite contents are chemically indistinguishable. Similarly, dense and vesicular regions of the same clast have identical major element glass compositions. On the basis of these analyses, differences in the physical appearance of individual clasts, including color and vesicularity, are not attributable to compositional variation.

Dacite glass compositions are reported in Table 5 and shown on a Harker variation diagram in Fig. 2a. Comparison of the glass compositions of dacite surge material with those of climactic pumice glass (Table 5) shows that the microlite-free, pre-climactic dacite is very similar to the phenocryst-rich magma tapped during the climactic eruption described by Pallister et al. (1996). However, the dacite produced by pre-climactic events ("pre-climactic dacite") exhibits a range of glass compositions as a result of variable degrees of microlite

**Table 5** Average matrix glass compositions of Pinatubo dacite

sample event n	P301 [0.157] surge 3 8	P311 [0.134] surge 3 7	P321 [0.038] surge 3 7	P302 [0.018] surge 3 9	P053 [0.051] surge 3 <sup>1</sup> surge 3 <sup>2</sup> 4 5		P421 [0.096] surge 4 5	P501 [0.106] surge 5 9
SiO <sub>2</sub>	79.1 (0.4)	79.2 (0.4)	77.2 (0.2)	77.9 (0.3)	78.6 (0.3)	78.4 (0.4)	78.9 (0.5)	78.5 (0.4)
TiO <sub>2</sub>	0.15 (0.06)	0.17 (0.06)	0.17 (0.05)	0.12 (0.06)	0.10 (0.03)	0.12 (0.05)	0.13 (0.04)	0.12 (0.05)
Al <sub>2</sub> O <sub>3</sub>	10.5 (0.1)	11.1 (0.2)	11.9 (0.2)	11.7 (0.2)	12.1 (0.1)	12.0 (0.3)	11.6 (0.5)	11.4 (0.2)
MgO	0.11 (0.02)	0.10 (0.03)	0.18 (0.03)	0.16 (0.02)	0.28 (0.20)	0.18 (0.02)	0.16 (0.02)	0.15 (0.02)
CaO	0.45 (0.07)	0.64 (0.07)	1.04 (0.04)	0.93 (0.04)	0.96 (0.09)	0.94 (0.12)	0.92 (0.22)	0.77 (0.07)
MnO	0.05 (0.05)	0.03 (0.04)	0.04 (0.01)	0.05 (0.03)	0.08 (0.03)	0.04 (0.05)	0.03 (0.03)	0.04 (0.02)
FeO	0.69 (0.08)	0.79 (0.11)	0.83 (0.06)	0.70 (0.09)	0.93 (0.05)	0.68 (0.09)	0.82 (0.05)	0.77 (0.11)
Na <sub>2</sub> O	2.92 (0.23)	3.17 (0.19)	3.74 (0.24)	3.82 (0.24)	3.02 (0.31)	3.01 (0.27)	3.11 (0.13)	2.81 (0.18)
K <sub>2</sub> O	3.97 (0.18)	3.49 (0.14)	3.14 (0.05)	3.19 (0.06)	3.13 (0.08)	3.06 (0.17)	2.98 (0.19)	3.16 (0.21)
Cl	0.12 (0.02)	0.11 (0.01)	0.12 (0.02)	0.12 (0.02)	n.a.	n.a.	0.11 (0.01)	0.14 (0.03)
total	98.1 (0.6)	98.8 (0.6)	98.4 (0.4)	98.6 (0.5)	99.2 (0.3)	98.4 (0.5)	98.8 (0.5)	97.9 (0.5)
sample event n	P511 [0.051] surge 5 9	P611 [0.013] surge 6 7	P612 [0.117] surge 6 9	P613 [0.218] surge 6 10	P701 [0.091] surge 7 7	P801 [0.001] surge 8 7	P101 [0.013] surge 8 <sup>1</sup> surge 8 <sup>2</sup> 4 4	
SiO <sub>2</sub>	77.8 (0.4)	77.3 (0.1)	78.2 (0.7)	79.5 (0.7)	78.2 (0.3)	77.3 (0.3)	77.5 (0.2)	78.0 (0.4)
TiO <sub>2</sub>	0.12 (0.03)	0.13 (0.10)	0.20 (0.06)	0.28 (0.08)	0.12 (0.05)	0.12 (0.03)	0.11 (0.03)	0.14 (0.04)
Al <sub>2</sub> O <sub>3</sub>	11.7 (0.1)	11.8 (0.1)	11.2 (0.1)	10.1 (0.6)	11.6 (0.3)	12.0 (0.1)	12.1 (0.1)	12.2 (0.1)
MgO	0.17 (0.02)	0.17 (0.02)	0.10 (0.03)	0.21 (0.14)	0.14 (0.03)	0.19 (0.02)	0.18 (0.04)	0.17 (0.05)
CaO	1.01 (0.04)	1.06 (0.05)	0.65 (0.09)	0.62 (0.33)	0.82 (0.17)	1.12 (0.06)	1.07 (0.02)	1.02 (0.03)
MnO	0.04 (0.04)	0.05 (0.03)	0.03 (0.03)	0.04 (0.04)	0.05 (0.02)	0.03 (0.02)	0.01 (0.01)	0.01 (0.02)
FeO	0.83 (0.07)	0.71 (0.09)	0.90 (0.09)	0.69 (0.19)	0.84 (0.12)	0.82 (0.06)	0.75 (0.13)	0.71 (0.02)
Na <sub>2</sub> O	3.59 (0.27)	3.87 (0.11)	2.78 (0.34)	2.25 (0.26)	3.31 (0.34)	3.96 (0.19)	3.56 (0.03)	3.13 (0.15)
K <sub>2</sub> O	3.08 (0.12)	3.16 (0.08)	3.18 (0.51)	3.03 (0.36)	3.54 (0.26)	3.10 (0.07)	3.13 (0.04)	3.05 (0.07)
Cl	0.13 (0.02)	0.10 (0.02)	0.15 (0.02)	0.16 (0.02)	0.14 (0.02)	0.12 (0.02)	n.a.	n.a.
total	98.4 (0.4)	98.4 (0.3)	97.4 (0.5)	96.9 (0.5)	98.8 (0.5)	98.7 (0.4)	98.5 (0.2)	98.4 (0.5)
sample event n	P102 [n.a.] surge 8 7	P103 [0.053] surge 8 7	P901 [0.011] surge 9 7	P121 [n.a.] climactic PR 13	P111 [n.a.] climactic PP 13	EW910615-1* climactic PR 24	PH13D* climactic PP 6	
SiO <sub>2</sub>	78.5 (0.7)	78.2 (0.5)	77.3 (0.3)	77.5 (0.9)	74.2 (2.6)	76.7 (0.8)	72.7 (1.4)	
TiO <sub>2</sub>	0.09 (0.09)	0.15 (0.02)	0.12 (0.03)	0.10 (0.04)	0.21 (0.08)	0.06 (0.03)	0.16 (0.10)	
Al <sub>2</sub> O <sub>3</sub>	11.8 (0.3)	11.7 (0.0)	11.9 (0.1)	12.6 (0.2)	13.4 (0.9)	12.6 (0.2)	13.6 (1.1)	
MgO	0.24 (0.08)	0.17 (0.03)	0.19 (0.02)	0.26 (0.13)	0.75 (0.53)	0.10 (0.02)	0.75 (0.53)	
CaO	0.87 (0.19)	0.98 (0.04)	1.11 (0.04)	1.19 (0.06)	2.22 (0.83)	1.20 (0.04)	2.35 (0.91)	
MnO	0.03 (0.02)	0.04 (0.03)	0.04 (0.03)	0.05 (0.03)	0.06 (0.04)	n.a.	n.a.	
FeO	0.85 (0.08)	0.74 (0.06)	0.80 (0.13)	0.83 (0.13)	1.61 (0.52)	0.74 (0.04)	1.67 (0.72)	
Na <sub>2</sub> O	2.98 (0.26)	3.29 (0.10)	3.85 (0.10)	2.89 (0.69)	2.93 (0.48)	3.66 (0.62)	3.74 (0.75)	
K <sub>2</sub> O	3.30 (0.18)	3.05 (0.18)	3.10 (0.04)	3.03 (0.10)	2.78 (0.28)	3.07 (0.20)	2.75 (0.23)	
Cl	n.a.	0.11 (0.01)	0.11 (0.02)	n.a.	n.a.	n.a.	n.a.	
total	98.6 (0.1)	98.4 (0.5)	98.5 (0.2)	98.4 (1.0)	98.2 (1.1)	98.1 (1.0)	97.6 (2.1)	

[ ] = microlite volume fraction,  $\phi$ . Values are sample averages. ( ) =  $1\sigma$

<sup>1</sup> Dense portion of clast

<sup>2</sup> Vesicular portion of clast. Unless noted, samples are homogeneous

n.a. = not analyzed. \* data from Pallister et al. 1996

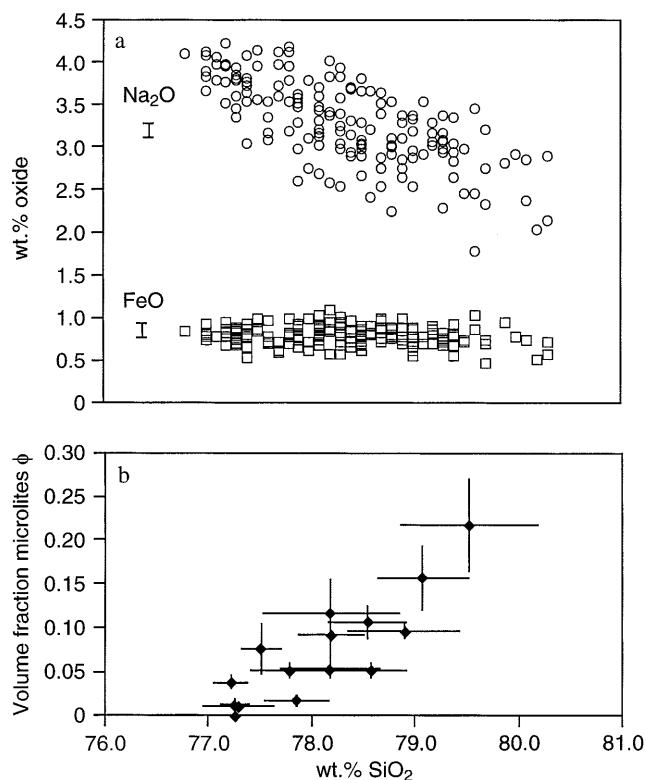


**Fig. 2** **a** Harker variation diagram for pre-climactic Pinatubo dacite glasses, showing weight percent Na<sub>2</sub>O and FeO vs SiO<sub>2</sub>. Vertical error bars represent analytical uncertainty for Na<sub>2</sub>O and FeO. The analytical error for SiO<sub>2</sub> is  $\pm 1.6$  wt.%. **b** Average clast microlite content,  $\phi$ , vs average clast SiO<sub>2</sub> content. Error bars in both directions represent  $1\sigma$  of average for all analyses in that clast (see Tables 2, 5)

crystallization. For example, SiO<sub>2</sub> increases from 77.2 to 79.5 wt.%, whereas Na<sub>2</sub>O decreases from 3.96 to 2.25 wt.%, due to the growth of plagioclase microlites. Microlite content (see Appendix C) is plotted against glass SiO<sub>2</sub> content (Fig. 2b) to illustrate the effect of crystallization on liquid composition.

### Feldspar microlites

Microlites less than 3  $\mu\text{m}$  in length could not be analyzed; thus, probing was limited to dacite clasts with the largest crystals, which were also the most crystalline clasts (P301, P311, P612, P613). The beam was centered on the crystals in order to minimize incorporation of the surrounding glass into the analysis volume. Therefore, analyses represented either the core composition or an integrated average microlite composition, depending on the relative sizes of the spot and microlite (and the location of the two-dimensional cut through the crystal). Compositions range from Or<sub>2</sub>Ab<sub>66</sub>An<sub>32</sub> to Or<sub>1</sub>Ab<sub>34</sub>An<sub>65</sub>, encompassing the range of microlite compositions reported for the phenocryst-rich climactic dacite (An<sub>38</sub>–An<sub>53</sub>; Pallister et al. 1996). Selected analyses are given in Table 6.

### H<sub>2</sub>O<sub>T</sub> content

Dense dacite clasts were selected for FTIR analysis so that the full range in microlite content and eruptive parameters were represented (see Table 2). Average H<sub>2</sub>O<sub>T</sub> contents from the 11 clasts analyzed are reported in Table 3. The H<sub>2</sub>O<sub>T</sub> concentrations among all of the analyses range from 0.77 to 2.06 wt.%, with clast averages spanning a relatively narrow range from 1.13–1.66 wt.%. There was no correlation between H<sub>2</sub>O<sub>T</sub> and microlite crystallinity, repose interval duration, or timing in eruptive sequence.

### Textures

#### Qualitative observations

Phenocryst-rich climactic dacite is texturally uniform and is qualitatively similar in vesicle structure to other plinian pumices (e.g., Heiken and Wohletz 1987; Houghton and Wilson 1989; Klug and Cashman 1994, 1996). Texturally and compositionally identical dacite is also present in pre-climactic deposits. Vesicles in this material are characterized by smooth walls that thin to several microns and span a wide range of sizes (Fig. 3a, b). In contrast, phenocryst-poor material is microlite-bearing and contains thicker, rough vesicle walls (Fig. 1f).

As indicated by the large variation in clast density, surge material contains a spectacular range of vesicle shapes, sizes, and spatial distributions. Within the highest-density clasts, vesicles commonly occur in clusters that appear to have quenched while in the process of expanding as fronts (Fig. 3c), or where bounded by phenocrysts (Fig. 3d). Another variant in the densest material is the presence of relatively large, isolated vesicles surrounded by dense glass (Fig. 3e). In contrast, some of the less dense clasts have a relatively uniform spatial distribution of similarly sized, thick-walled vesicles (Fig. 3f). In heterogeneously vesicular clasts, no differences in microlite content or characteristics were observed in the vicinity of vesicles.

Inspection of vesicle-free areas of dense dacite clasts shows that small elongate feldspar microlites are commonly oriented by flow. While the preferred orientation of microlites varies over short-length scales, e.g., in the vicinity of larger crystals, the overall distribution of orientations appears to be random over the centimeter scale of clasts (Fig. 1d, e). The spatial distribution of microlites becomes less homogeneous as groundmass crystallinity increases. Concentrations of microlites occur in the vicinity of some phenocrysts. The fact that the glass composition is the same in the microlite-rich and microlite-poor areas suggests that filter pressing by large phenocrysts concentrates microlites in the vicinity of those crystals (Fig. 4a, b). Biotite phenocrysts record stress in the magma at the time of quench, through breaking or bending along cleavage planes (Fig. 4c, d).

**Table 6** Representative feldspar compositions from Pinatubo dacite

sample spot size ( $\mu\text{m}$ )	P301 8	P301 5	P301 n.r.	P301 5	P311 2	P311 3	P311 5	P311 3
SiO <sub>2</sub>	54.4	59.8	54.7	65.3	59.8	59.3	50.9	53.8
Al <sub>2</sub> O <sub>3</sub>	27.9	25.5	29.3	21.0	23.3	23.9	28.8	26.9
FeO	0.63	0.34	0.62	0.32	0.26	0.25	0.57	0.67
CaO	10.74	7.72	11.94	4.02	6.44	7.15	13.00	10.67
Na <sub>2</sub> O	5.23	6.72	4.51	7.59	7.28	7.35	3.79	5.09
K <sub>2</sub> O	0.26	0.45	0.26	1.19	0.39	0.43	0.17	0.25
total	99.1	100.5	101.3	99.3	97.5	98.3	97.2	97.4
$\Sigma$ (cations)	5.00	4.97	4.98	4.91	4.97	5.00	4.99	4.99
Ab	46.1	59.6	40.0	71.6	65.6	63.4	34.2	45.6
An	52.4	37.8	58.5	21.0	32.1	34.1	64.8	52.9
Or	1.5	2.6	1.5	7.4	2.3	2.4	1.0	1.5

sample spot size ( $\mu\text{m}$ )	P612 4	P612 6.5	P612 2.5	P612 3	P613 5	P613 18	P613 n.r.	P613 15
SiO <sub>2</sub>	62.3	56.1	61.3	58.7	57.5	54.0	51.6	55.5
Al <sub>2</sub> O <sub>3</sub>	24.3	27.7	24.1	26.1	26.7	28.5	30.2	27.2
FeO	0.64	0.56	0.40	0.56	0.82	0.78	0.65	0.67
CaO	7.23	10.34	6.83	8.68	9.86	11.07	12.81	9.71
Na <sub>2</sub> O	6.13	5.58	6.73	6.35	5.89	4.84	3.96	5.42
K <sub>2</sub> O	0.62	0.30	0.55	0.36	0.41	0.27	0.14	0.44
total	101.2	100.6	99.9	100.8	101.2	99.4	99.3	99.0
$\Sigma$ (cations)	4.91	5.00	4.94	4.98	4.99	4.99	5.00	4.99
Ab	58.2	48.6	61.9	55.8	50.7	43.5	35.6	48.9
An	37.9	49.7	34.7	42.1	46.9	54.9	63.6	48.4
Or	3.9	1.7	3.3	2.1	2.3	1.6	0.8	2.6

n.r. = not recorded

Other, less flexible, phenocryst phases occur primarily as broken fragments (bright mafic minerals and gray plagioclase in Fig. 3c). In some instances the fragments are separated by only a few microns. In general, however, the pieces are too scattered for visual reconstruction.

The most abundant microlite phase by volume is feldspar. Feldspar morphology changes with increasing groundmass crystallinity. Acicular, skeletal, and hopper forms shown in Fig. 4e may be contrasted with the larger, slightly zoned, more equant crystals in Fig. 4f. Small, equant mafic phases that appear white on these backscattered electron (BSE) images include Fe–Ti oxides and pyroxene. Although biotite and hornblende are present as (pristine) phenocryst phases (Figs. 3e, 4c, d), no microlites of hydrous phases were observed.

Several clasts from throughout the eruptive sequence contain microlites of an anhedral phase of SiO<sub>2</sub>. In some instances the microlites appear engulfed in silica (Fig. 4g); in other cases the silica phase is surrounded by feldspar (Fig. 4h). Clasts bearing these crystals tend to have a high feldspar microlite crystallinity. It is not clear whether this phase represents incipient devitrification (as noted in Cashman 1992), partially resorbed vapor-phase crystals grown when the magma was inflated and vesicular (as in Hoblitt and Harmon

1993), or pseudo-eutectic crystallization at high degrees of supersaturation. Given that these textures constitute ambiguous information about the order of crystallization of feldspar and the silica phase, and the observation that the silica phase is only present in the most crystalline samples, the most likely explanation may be simultaneous crystallization of these phases from an evolved liquid. The CIPW norm of microlite-free preclimactic glass is 55% feldspar and 45% quartz. Therefore, expressed in terms of crystallization potential, the most crystalline groundmass observed represents ~40% of the normative feldspar content, whereas the amorphous silica phase is estimated to represent  $\leq 5\%$  of the normative quartz content.

#### Quantitative observations

Clast density and microlite content, crystal number density, and crystal size are inter-related. All low-density clasts are microlite poor, whereas the microlite content of high-density clasts spans the entire range of microlite contents observed (Fig. 1c–e). For this reason, the textural investigation was conducted primarily on the high-density clasts. Although a substantial range in microlite characteristics is present among the surge

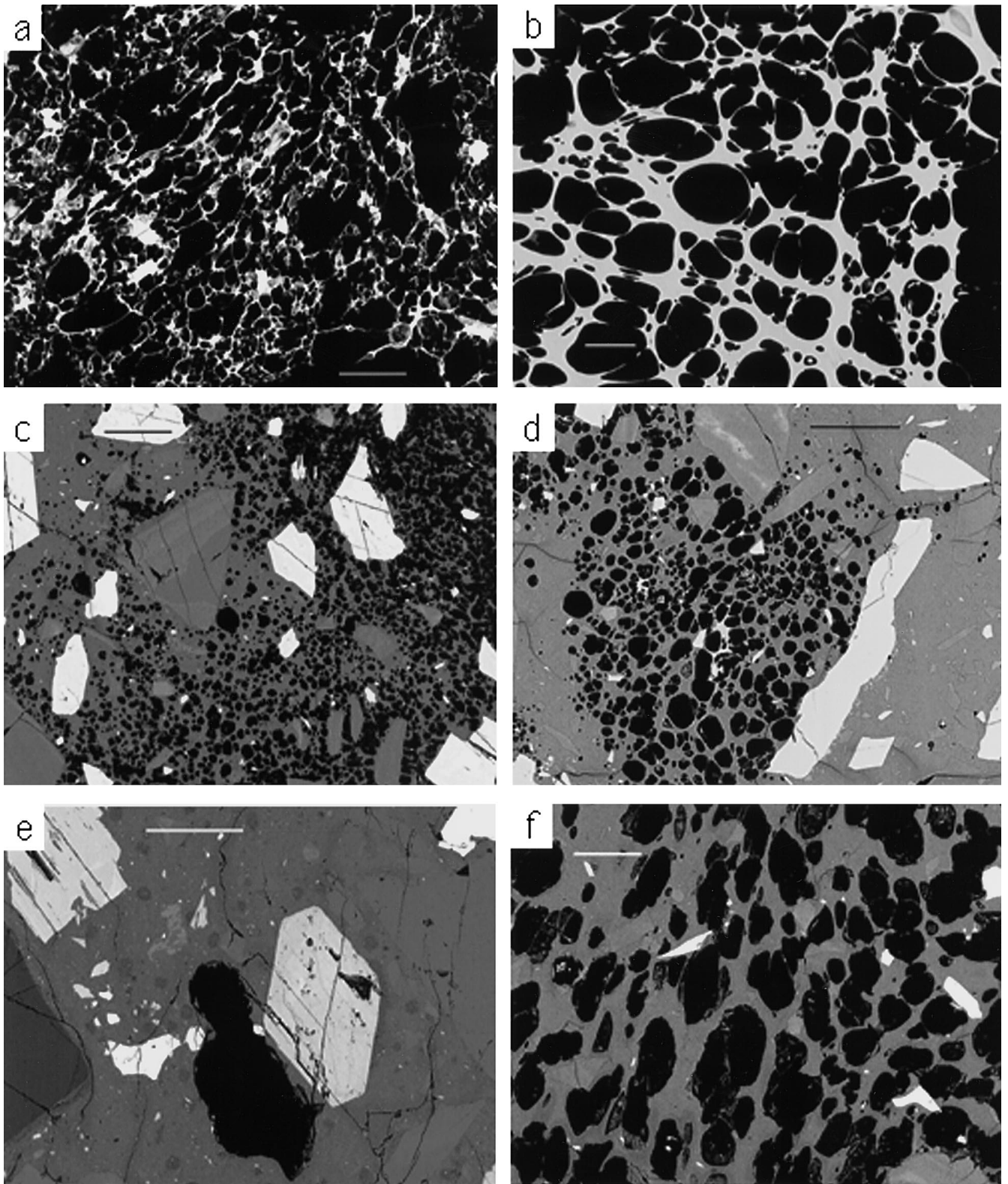


**Fig. 3a–f** Vesicle textures in pre-climatic Pinatubo dacite. *Scale bars* are 100 µm long, except in **b**, where *scale bar* represents 10 µm. **a, b** Low-density pumice. Phenocrysts appear in low-magnification BSE images as light-colored clots in **a**; glass interstices

are microlite free (**b**). **c, d** Vesicle concentration surrounded by dense glass. **e** A large isolated vesicle adjacent to hornblende phenocryst. **f** Homogeneous distribution of similarly sized vesicles

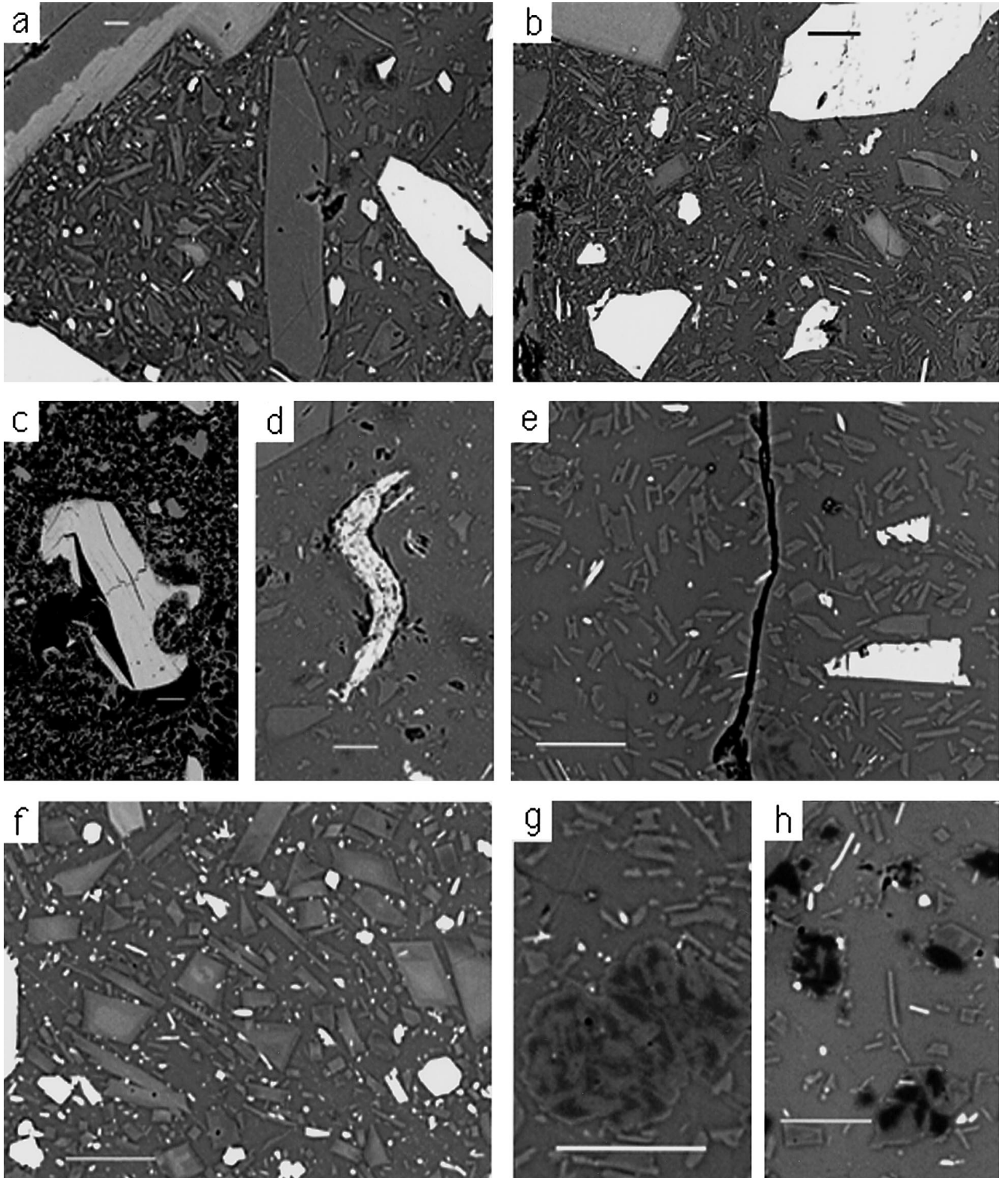


**Fig. 4a–h** Microlite textures in Pinatubo dacite. *Scale bars* are 10  $\mu\text{m}$ , except in **c**, where *scale bar* represents 100  $\mu\text{m}$ . **a, b** Inhomogeneous distribution of feldspar microlites in highly crystalline clast, possibly a result of filter pressing. **c, d** Shattering and bending of biotite phenocrysts. **e** Skeletal and hopper-shaped microlites. The elongate appearance of microlites in thin section indi-

cates that the three-dimensional morphology is tabular. **f** Large-zoned microlites. More equant in thin section, their three-dimensional shape is prismatic. **g, h** Dark areas are an unidentified  $\text{SiO}_2$  phase. In **g** microlites appear to be engulfed by this phase. In **h** feldspar is intergrown with it

clasts studied, most individual clasts are homogeneous enough to be characterized by measured areal microlite-number density ( $N_A$ ), volume fraction ( $\phi$ ), and average size,  $s_n$  (summarized in Table 2). Microlite-number densities span nearly three orders of magnitude among the surge samples analyzed, from 842 to  $>152,000 \text{ mm}^{-2}$ . These values encompass the entire range observed in other silicic magmas for which detailed microlites textures have been compiled: 2000–10,000  $\text{mm}^{-2}$  for 1989–1990 Redoubt (Wolf and Eichelberger 1997), 75,000  $\text{mm}^{-2}$  for Unzen (Nakada and Motomura 1995), and 2000–90,000  $\text{mm}^{-2}$  for Rock Mesa, Oregon (Rogers 1996). Groundmass feldspar crystallinity is also quite variable, ranging from 0 to 0.22 of the groundmass.

Although  $N_A$  and  $\phi$  vary significantly among samples, they do not vary independently. Microlite sizes are relatively uniform: the average microlite size computed as a combination of  $N_A$  and  $\phi$  (see Appendix C) among clasts ranges from 0.49 to 1.80  $\mu\text{m}$ . The overall average size for the  $\approx 33,000$  crystals counted from all of the clasts is 0.91  $\mu\text{m}$  ( $1\sigma=0.12$ ), indicating that 68% of the  $N_A$ - $\phi$  ratios fall between  $1.59 \times 10^6$  to  $9.57 \times 10^5$  (Fig. 5). Since mean crystal size is a formulation of  $N_A$  and  $\phi$ , these ratios are equivalently expressed in Fig. 5 as lines of constant mean crystal size, corresponding to 0.79 and 1.02  $\mu\text{m}$ , respectively. Movement over time along one of these lines indicates that crystallinity is in-

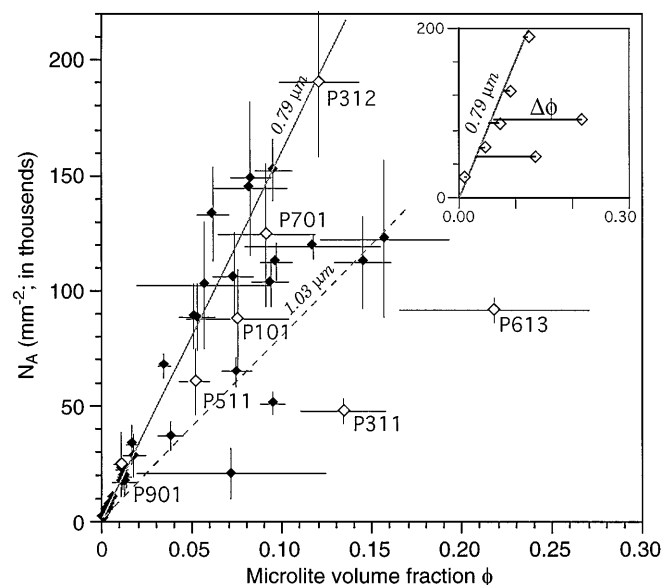


**Fig. 5** Microlite volume fraction ( $\phi$ ) and area number density ( $N_A$ ). 68% of all microlites lie between the *solid line* and *dashed line* representing 0.79 and 1.03  $\mu\text{m}$  (average size  $\pm 1\sigma$ , respectively). *Open symbols* represent clasts selected for detailed shape and size distribution study. *Inset* shows those selected clasts plotted with respect to the 0.79- $\mu\text{m}$  line. The difference between the clast  $\phi$  and the reference value of  $\phi$  (given by the *solid line*) for a given value of  $N_A$  is  $\Delta\phi$ , an indicator of crystallization regime. Large  $\Delta\phi$  indicates that crystallization was dominated by growth on existing sites, whereas small  $\Delta\phi$  indicates that nucleation of new crystals dominated

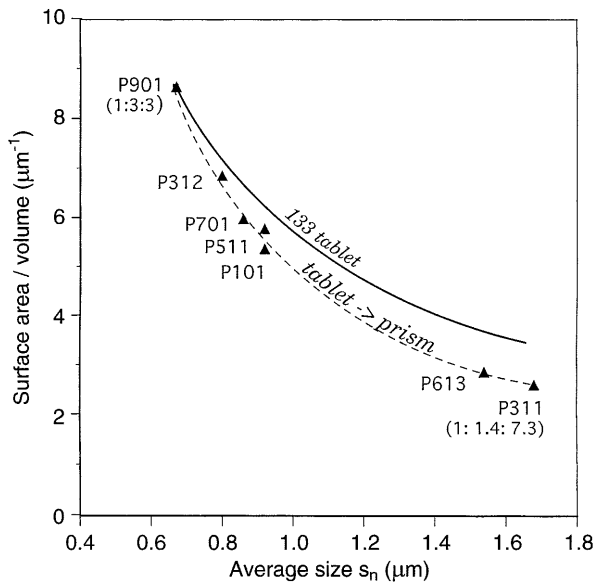
creasing chiefly by introduction of new crystals of the same average size. The solid line in Fig. 5 may represent a lower limit to observable size, so that in a practical sense, points falling along this line represent a nucleation-dominated crystallization regime. In contrast, points falling to the right of the dashed line reflect a crystallization history dominated by growth on existing sites rather than nucleation of new crystals. The solid line and clasts for which more detailed textural analysis was performed are replotted in the inset graph of Fig. 5.  $\Delta\phi$  is defined as the difference between the clast  $\phi$  and the value of  $\phi$  dictated by the solid line for the given value of  $N_A$ , and is a measure of the extent that crystallinity is increasing by crystal growth: small  $\Delta\phi$  represents nucleation-dominated crystallization, whereas large  $\Delta\phi$  indicates a growth-dominated regime.

It is clear from Fig. 4e and f that crystal shape also varies significantly among clasts of pre-climactic dacite. However, it may not be obvious from the images, which are two-dimensional slices, how the variation corresponds to change in three-dimensional form. Given the time-consuming nature of shape characterization (see Appendix C), seven clasts were selected for analysis and  $\Delta\phi$ . The clasts chosen, P101, P311, P312, P501, P613, P701, and P901 were deposited by surges 1, 3, 5, 6, 7, and 9, respectively. Although clast densities range from 2260 to 2580  $\text{kg m}^{-3}$ , these clasts represent the full observed range in microlite size,  $\phi$ ,  $N_A$ , and eruptive parameters (Fig. 5; Tables 1, 2). Average crystal shape information is listed in Table 7. Based on the statistical distribution of crystal breadth to length ratios (Higgins 1994) measured from BSE images, average crystal habits for these samples were determined to range from uniaxial tablets (dimensions of  $\approx 1:3:3$ ) to elongate prisms ( $\approx 1:1:7$ ). Since crystals are most likely to be intersected along planes perpendicular to their longest dimensions, the tablets and prisms appear in thin section as high-aspect ratio needles and low-aspect ratio rectangles, respectively (Fig. 4). Average size ( $s_n$ ) is correlated with average shape, so that the smallest, high  $N_A$  microlites are tablet shaped, whereas the larger microlites from more crystalline samples are prismatic. The transition from small tablet to larger prism represents a decrease in the surface area to volume ratio (SA/vol) from 8.65 to 2.62  $\mu\text{m}^{-1}$ , or  $\sim 70\%$  (Fig. 6). For comparison, growth of a 1:3:3 tablet resulting in a similar change in size without a change in shape would result in a decrease in SA/vol of 60%.

Crystal size distributions (CSDs) were obtained for the same seven clasts (Fig. 7). Application of the Peterson (1996) correction technique computed using the average shape information yielded linear distributions in size- $\ln n$  (population density) space over most of the sizes represented. Population densities for the smallest size classes ( $<1\text{--}2 \mu\text{m}$ ) fell below the linear trend defined by the larger classes. Because this is likely a consequence of poor resolution of the smallest crystals, the small-size information was not included in the calcula-

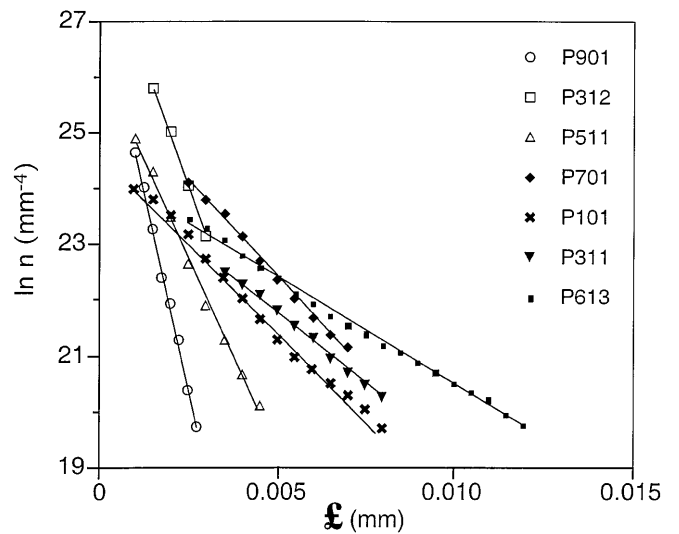
**Table 7** Microlite shape and size data

sample no.	no. crystals	time <sup>1</sup> (s)	shape (S=1)			Parameters calculated from CSD plots								
			I	L	habit	avg. size <sup>2</sup> (mm)	area number density <sup>2</sup> N <sub>A</sub> (mm <sup>-2</sup> )	vol. number density (mm <sup>-3</sup> )	$\phi^3$	$\phi^2$	growth rate (mm s <sup>-1</sup> )	nucleation rate (no. mm <sup>-3</sup> s <sup>-1</sup> )		
P101	343	7440	2.22	4.63	prism	1.6E-03	<i>9.0E-04</i>	1.2E+05	<i>8.8E+04</i>	7.8E+07	0.19 (0.14)	<i>0.07</i>	2.1E-07	1.1E+04
P311	223	15720	1.45	7.33	prism	1.9E-03	<i>1.7E-03</i>	1.4E+05	<i>4.7E+04</i>	7.1E+07	0.08 (0.05)	<i>0.13</i>	1.2E-07	4.5E+03
P312	483	15720	2.97	4.00	tablet	5.6E-04	<i>1.0E-03</i>	7.4E+05	<i>1.9E+05</i>	1.3E+09	0.26 (0.20)	<i>0.12</i>	3.6E-08	8.4E+04
P511	321	4740	2.46	3.45	tablet	7.1E-04	<i>9.2E-04</i>	1.3E+05	<i>6.1E+04</i>	1.8E+08	0.08 (0.07)	<i>0.05</i>	1.5E-07	3.8E+04
P613	245	10440	1.41	6.40	prism	2.6E-03	<i>1.5E-03</i>	2.5E+05	<i>9.2E+04</i>	9.5E+07	0.34 (0.23)	<i>0.22</i>	2.5E-07	9.1E+03
P701	329	7920	2.86	6.04	prism	1.5E-03	<i>8.5E-04</i>	3.5E+05	<i>1.2E+05</i>	2.4E+08	0.35 (0.25)	<i>0.09</i>	1.8E-07	3.0E+04
P901	276	1680	3.03	3.03	tablet	3.5E-04	<i>6.5E-04</i>	1.1E+05	<i>2.4E+04</i>	3.0E+08	0.03 (0.03)	<i>0.01</i>	2.1E-07	1.8E+05

<sup>1</sup> repose interval duration<sup>2</sup> values in italics determined from direct image analysis<sup>3</sup> CSD parameters determined for  $\xi = [0 \text{ to } \infty]$  except for ( ), where  $\xi = [0 \text{ to maximum observed size}]$ **Fig. 6** Surface-area-to-volume ratio for clasts (triangles). Upper curve (ratio  $5.77*s_n^{-1}$ ) shows how this ratio changes as a 133 tablet grows. Dashed curve (ratio  $5.05*s_n^{-1.3}$ ) demonstrates additional reduction in surface-area-to-volume ratio due to shape change (from 1:3:3 to 1:1.4:7.3) during growth

tion of slope and intercept. Full CSDs for two of the clasts are presented in Appendix C, along with CSDs calculated without applying the shape correction technique. Although the methods yield similar CSD slopes, the shape-corrected data differ in the values of  $\ln n$ . For the tabular crystals of clast P901, the shape-correction slightly increases the frequency of crystals in the larger-size classes. The correction results in lower  $\ln n$  values for the prismatic crystals of clast P613.

Slopes, intercepts, and rates of crystal growth and nucleation derived from CSDs are listed with characteristic microlite shape in Table 7. Clasts P901 and P312, having tabular microlites, fall nearest to the solid line defined by  $\Delta\phi=0$  (Fig. 5). The microlite populations in these clasts have the smallest average sizes (greatest CSD slopes) and greatest rates of nucleation (largest CSD intercepts) among the selected subset of clasts. In

**Fig. 7** Crystal size distributions (CSDs) for selected clasts. Linear fits to data are used to extract crystal nucleation and growth rates. Open symbols represent clasts with tabular microlite shapes, filled symbols have prismatic crystals

contrast, clasts P311 and P613, with the largest  $\Delta\phi$  values, are characterized by prismatic microlites. The crystal populations in these clasts display the greatest average size and highest rates of crystal growth. The remaining clasts (P511, P101, and P701) have microlite shapes intermediate between tabular and prismatic, are characterized by intermediate  $\Delta\phi$  values, and have moderate CSD slopes and intercepts.

## Discussion

We suggest that the textural and compositional data presented previously may be used to (a) infer the timing of pre-eruptive volatile loss and crystallization in the Pinatubo dacite, (b) examine the dynamics of microlite crystallization, and (c) consider the possible feedback of these processes on eruptive style.

### Timing of volatile loss and microlite crystallization

By comparing the textural characteristics,  $H_2O$  contents, and observations of eruptive parameters, hypotheses concerning the timing of devolatilization and microlite crystallization during the pre-climactic blasts may be tested. Both repose intervals and eruption durations varied by approximately a factor of ten during the pre-climactic events (28–262 and 3–23 min, respectively), with no apparent correlation between the two (see Table 1). The timing of crystallization and volatile loss may be inferred if microlite and  $H_2O$  data consistently relate to either of these time scales. The  $H_2O_T$  contents of Pinatubo dacite glasses are intriguing, both for the values themselves and the relative homogeneity of values among eruptive events. Analyses indicate that the clasts are neither totally degassed to atmospheric values (0.1 wt.%) nor representative of magma chamber conditions (>5 wt.%; Rutherford and Devine 1996). If  $H_2O$  concentrations represent equilibrium solubilities, the pressures that correspond to the  $H_2O_T$  contents observed in the samples are 7.9–15.4 MPa (Burnham and Davis 1974), or approximate depths of 600–300 m (assuming overburden density of  $2650 \text{ kg m}^{-3}$ ). These  $H_2O_T$  values suggest that exsolution ceased at some level between the magma chamber and the surface. Instead of correlating with any particular eruptive time scale, the apparent homogeneity of the denser clasts implies that a similar process formed them during all of the events studied.

In contrast, microlite textures vary significantly. There appears to be no relationship between crystallinity and eruptive duration, column height, or the sequential order of eruptions. However, the maximum crystallinity observed in the material from a given event is correlated to the repose interval duration preceding that event (Figs. 8, 9). The most striking comparison is between the early events, which typically followed the longest repose intervals, and the late events, which followed the shortest repose intervals. The maximum crystallinities ( $\phi_{\max}$ ) of long-repose events are approximately ten times greater than those of short-repose events (Fig. 8). Figure 9 illustrates a point made previously, i.e., that all low-density clasts are microlite poor. It also illustrates that the crystallinity in denser clasts appears correlated with repose interval, as dense clasts from short-repose events contain no microlites, whereas dense clasts from long-repose events contain abundant microlites. It is important to note that although there is a correlation between  $\phi_{\max}$  and both clast density and repose interval (Fig. 9), many dense clasts from long-repose events have low microlite crystallinities (e.g., P321 and P611; Table 2). This variation in dense clasts from a single event, together with the observation that low-density, microlite-free dacite pumice was produced during all events (Hoblitt et al. 1996), indicates that portions of magma having experienced a range of degassing and crystallization histories were sampled during each discrete event. Therefore,

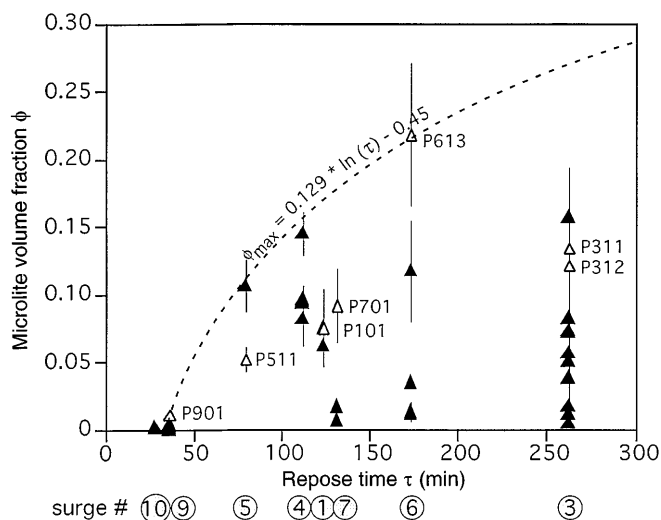


**Fig. 8** Microlite volume fraction vs repose time. Following an apparent nucleation time lag of approximately 40 min, the maximum crystallinity observed in each surge deposit ( $\phi_{\max}$ ) increases as a function of repose interval duration. That the rate of increase appears to diminish with time ( $\phi_{\max}$  vs time is fit with a logarithmic function) suggests that crystallization occurs in response to a discrete saturation event. Open triangles represent clasts selected for detailed microlite shape and size determination

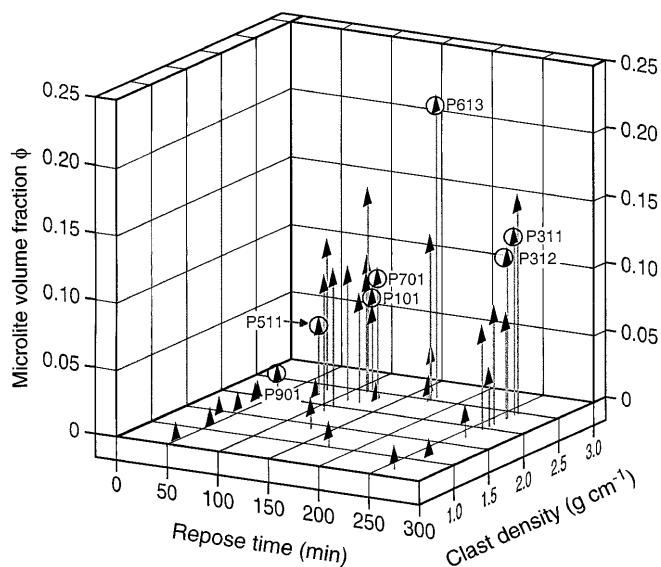


**Fig. 9** Repose time, clast density, and microlite content. Plot shows the relationship between macro- and microscopic characteristics and an eruptive parameter. All low-density clasts and clasts produced by short-repose events are microlite free. The greatest microlite content occurs in high-density clasts produced by long-repose events. Circles represent clasts selected for detailed microlite shape and size determination

$\phi_{\max}$  values describe an envelope that is used throughout the following analysis to infer the dynamics of crystallization in relation to eruptive parameters.

What is the sequence of eruptive processes that can result in these textures and volatile contents? The correlation of microlite textural characteristics with repose

interval duration (Figs. 8, 9) suggests that crystallization occurred between eruptions. However, the relative homogeneity of  $H_2O_T$  contents among these clasts ( $1.45 \pm 0.15$ ), regardless of repose interval duration or microlite content, suggests that each parcel of magma experienced a similar degassing history during ascent.

For the purposes of this discussion, we consider two processes that occur in sequence: volatile exsolution (devolatilization) and gas-phase separation from the magma (degassing). The first process profoundly changes the thermodynamic properties of the liquid (e.g., molar volume and liquidus temperature) and results in a bubbly two-phase suspension having greatly reduced density and modified rheology (Hess and Dingwell 1996) from the original solution. This process also changes phase stabilities, instigating microlite growth (Geschwind and Rutherford 1995, Swanson et al. 1989) and breakdown of hydrous phases, if present (Rutherford and Hill 1993). The second process is the physical separation of the volatile phase from the lava, which likely occurs through a network of interconnected bubbles (e.g., Eichelberger et al. 1986; Klug and Cashman 1996), as gas loss by flow through a permeable network will be much more efficient than gas loss by diffusion to a free surface.

When the rate of gas separation is commensurate with the rate of exsolution, the system undergoes open-system degassing (Eichelberger et al. 1986). For example, gas separation from subsurface magma under open-system conditions is commonly demonstrated by fumarolic degassing. Alternatively, the style of degassing may switch between open and closed as in the 1989–1990 explosive to effusive eruptions of Redoubt Volcano, Alaska (Wolf and Eichelberger 1997), spatter-rich pyroclastic flow deposits of Santorini, Greece (Mellors and Sparks 1991), and the massive effusive eruption of Quizapu, Chile (Hildreth and Drake 1992). Conversely, closed-system degassing implies that the exsolved phase remains in contact with melt. Explosive eruptions such as the 1340 AD subplinian activity of Mono Craters, California, resulted from dominantly closed-system conditions in which expansion of the exsolved phase accelerated the mixture out of the conduit before separation could occur (Newman et al. 1988).

The pattern of activity of Mt. Pinatubo, consisting of sporadic explosive events separated by intervals of seismic repose and quiescent gas emission, suggests that degassing occurred under a combination of open- and closed-system conditions. The fact that each event produced a substantial amount of vesicular pumice indicates that a portion of the erupted magma did not experience significant pre-eruptive volatile loss. Presumably, this magma underwent closed system, syn-eruptive gas exsolution and fragmentation. However, the presence of dense, partially degassed clasts in each of the surge deposits suggests that pre-eruptive gas loss occurred in at least part of each erupted magma batch. One possibility is that devolatilization of unerupted magma occurred within the conduit during each explo-

sive event. Syn-eruptive vesiculation could thus create a gas-permeable structure at a conduit level below the fragmentation surface that would facilitate post-eruptive volatile separation. This magma would therefore have experienced degassing under open-system conditions.

The observation that visible columns of ash and gas were emitted during repose intervals suggests that intra-eruptive separation of exsolved gases occurred readily. Equilibrium exsolution at depths of 300–600 m may explain why the  $H_2O$  contents are similar for all of the clasts analyzed despite the difference in repose interval duration. Syn-eruptive volatile separation from magma in the conduit has been proposed to cause transitions in eruptive style from effusive to intrusive (Eichelberger 1989; Eichelberger et al. 1986; Westrich et al. 1988), but examples of an *explosive*, syn-eruptive version of this process have not been recognized before.

#### Dynamics of devolatilization-induced crystallization

Volatile loss is the recognized driving force for crystallization in volcanic systems where eruptive time scales are short relative to the time necessary for sufficient cooling via conduction (Nakada and Motomura 1995; Swanson et al. 1989). For example, decompression experiments on Mount St. Helens dacite show that microlites can grow over time scales of magma ascent during effusive eruptions (4–8 days; Geschwind and Rutherford 1995). Syn-eruptive crystallization occurring over the time scales of explosive eruptions has not been documented previously, although isothermal decompression experiments using Mt. Pinatubo dacite demonstrate that feldspar microlites can grow in response to rapid decompressions from 220 to 50 MPa (e.g., M. J. Rutherford, pers. commun.). Although an experimental calibration of natural crystal textures with decompression/devolatilization rates does not yet exist, the kinetics of microlite growth in volcanic systems should resemble those in supercooled melts (e.g., Swanson 1977).

Textural data from Pinatubo clasts provide an unparalleled opportunity to study the early stages of crystallization in a natural, explosive silicic system. Each eruptive event drew from the same magma reservoir, so that the samples represent snapshots of the system at different times. Clasts produced by events that follow short repose intervals (<40 min) are microlite free (Fig. 8), suggesting a nucleation time lag between the supersaturating event and the system's crystallization response (e.g., Lasaga 1981; Lofgren 1980). This occurs because the kinetics of crystallization are more sluggish than those of exsolution, and even though feldspar is a stable phase in the partly devolatilized magma, nucleation and growth to appreciable volume fractions ( $\phi > 0.02$ ) is suppressed for at least 40 min. Comparison of textures with respect to repose interval durations shows that aft-

er the lag time is exceeded, number density and crystallinity rapidly increase (Fig. 8).

Several observations suggest that crystallization occurred following a single supersaturation event, and that the driving force for crystallization (reflected by nucleation rate; Swanson 1977) decreased with time following that event. For example, the most rapid crystal nucleation rate ( $1.8 \times 10^5 \text{ mm}^{-3} \text{ s}^{-1}$ ) is observed in a clast deposited by the ninth surge event, which was preceded by a very short repose interval (28 min), whereas the slowest crystal nucleation rate ( $4.5 \times 10^3 \text{ mm}^{-3} \text{ s}^{-1}$ ) is observed in a sample preceded by the longest repose interval (262 min). Note that these rates are minima since crystallization is presumed to occur over the entire repose interval. This simple relationship is complicated by the observation that in most cases a single event produced material representing a variety of crystallization histories. For example, the crystal size distribution of clast P312, also from the longest-repose event, records a moderately high nucleation rate ( $8.4 \times 10^4 \text{ mm}^{-3} \text{ s}^{-1}$ ). The textures represented in this clast may signify that devolatilization and resultant crystallization occurred shortly before the third surge-producing event, rather than immediately following the close of the second surge-producing event. A variety of crystal textures present within material from a single event (see Figs. 8, 9) could reflect a vertical stratification in the extent of gas loss and crystallization within conduit magma at the time of the eruption.

Comparison of  $N_A$  and  $\phi$  suggests that crystallizing magmas were initially dominated by nucleation, but that the growth of existing crystals eventually surpassed nucleation as the primary means of increasing crystallinity (Fig. 5). The maximum total microlite crystallinity observed in each event ( $\phi_{\text{max}}$ ), which incorporates nucleation and growth rates, may increase logarithmically with time (Fig. 8). While  $\phi_{\text{max}}$  increases with time,  $d\phi/dt$  decreases with time from  $\approx 0.003$  to  $\approx 0.001 \text{ min}^{-1}$ . These trends are consistent with results from crystallization experiments that show a change from nucleation-dominated crystallization to growth-dominated crystallization accompanying a decrease in supersaturation (Lofgren 1980; Muncill and Lasaga 1988; Swanson 1977).

Shape analysis of microlites may add support to this interpretation. A transition from tabular to prismatic morphology with increasing  $\phi$  resulted in a significant decrease in the ratio of surface area to volume beyond that of simple crystal growth (Fig. 6). In a comparative study of feldspar microlites and megacrysts within dacitic Kameni lavas (Greece), Higgins (1996b) determined that the microlites were tabular (1:5:6), whereas megacrysts were more blocky (1:3:4). This trend relating growing crystal size with increasingly equant crystal habit is similar to the correlation among Pinatubo microlites. However, differences in the Kameni crystal shapes were ascribed to differences in the dynamic crystallization environment (well-stirred vs static magma), rather than a decrease in the thermodynamic driv-

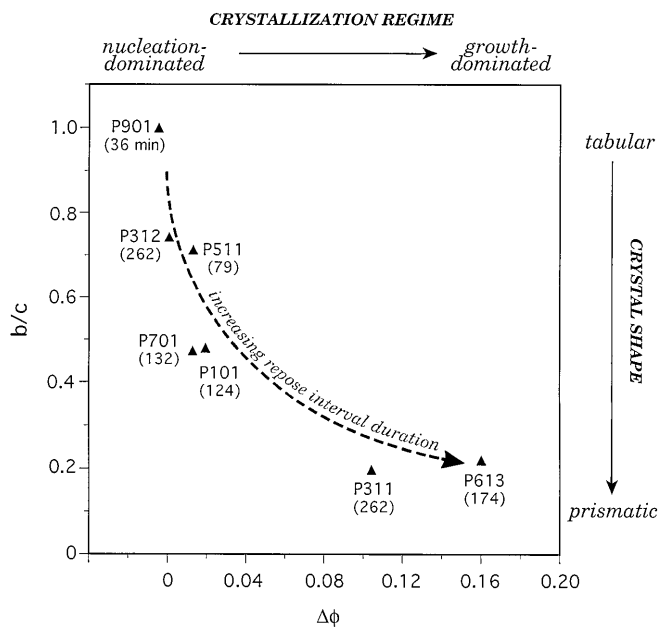


**Fig. 10** Crystallization regime and shape. Shape, characterized by the ratio of the intermediate to longest dimension, is correlated with nucleation- or growth-dominated crystallization regimes as expressed by  $\Delta\phi$  (see Fig. 5). As repose interval duration increases and equilibrium is approached, crystallization changes from nucleation dominated to growth dominated and shape evolves from tabular to prismatic

ing force with time. Since there is no basis for suspecting variation in the agitation of magma during the preclimactic eruptive sequence at Pinatubo, a chemical explanation seems more plausible in this case.

Changes in CSD with increasing time (and  $\phi$ ) may yield information on conditions under which crystallization occurred (Marsh 1988; Marsh 1998). Analytical solutions to the crystal population balance equations assuming batch crystallization indicate that over time CSDs maintain the same slope (average size) while  $n^\circ$  (nuclei density) increases, producing parallel CSDs with increasing intercept values (Marsh 1998). This progression may represent a system in which crystallization occurs at high supersaturations since crystallization is dominated by nucleation. The crystal textures (relationships among  $N_A$ ,  $\phi$ , and shape) of Pinatubo samples appear to indicate a progression in which the degree of supersaturation decreased in time, so that the style of crystallization switched from nucleation dominated to growth dominated. The CSDs from the Pinatubo samples consequently pivot from steep sloped with high intercepts (high nucleation rate) to shallow sloped with low intercepts (high growth rate) about a region defined by  $\ln n = \sim 23-24$  and  $L = \sim 2-5 \mu\text{m}$  (Fig. 7). Furthermore, distributions divided into groups (based on crystal shape) appear to correlate with the two nucleation and growth regimes also delineated by CSD parameters. Crystal size distributions from clasts P901, P511, and P312 (tabular crystal morphology) are

step ( $-1413$  to  $-2819$   $\text{mm}^{-1}$ ), whereas CSDs from the remaining clasts, (P701, P101, P311, and P613; prismatic microlites) are shallower ( $-385$  to  $-639$   $\text{mm}^{-1}$ ). The correlation of shape with CSD parameters reinforces the interpretation that the dynamics of growth changed over the  $\sim 270$ -min crystallization interval. Assuming that in general (therefore omitting P312), crystallization of these clasts occurred throughout the repose interval, characteristic crystal shapes and CSDs indicate that the switch in crystallization regime from nucleation dominated to growth dominated occurred between  $\sim 5000$  and  $\sim 8000$  s (1.3–2.2 h).

Crystal size distribution analysis of plagioclase microlites in dacite of the 1980–1986 dome eruptions of Mount St. Helens suggests growth rates from  $2.7 \times 10^{-8}$   $\text{mm s}^{-1}$  in 1980 to  $9.7 \times 10^{-11}$   $\text{mm s}^{-1}$  in later domes (Cashman 1992). The average Pinatubo feldspar microlite growth rate ( $1.7 \times 10^{-7}$   $\text{mm s}^{-1}$ ) is therefore approximately fifty times faster than the fastest estimated average growth rate of feldspar microlites in Mount St. Helens dacite, but similar to minimum growth rates of microlites observed in decompression experiments of Mount St. Helens dacite ( $7.2 \times 10^{-8}$  to  $1.4 \times 10^{-7}$   $\text{mm s}^{-1}$ ; Geschwind and Rutherford 1995). Both nucleation and growth rates increase with increasing supersaturation (Brandeis and Jaupart 1987; Cashman 1993; Kirkpatrick 1981). Thus, feldspar number density and size, which reflect overall kinetics, indicate relative supersaturation among these systems. The fact that the feldspar nucleation rates in subplinian events of Pinatubo are greater by five to nine orders of magnitude than accompanying effusion of Mount St. Helens dome lavas suggests that crystallization of Pinatubo magma occurred under more highly supersaturated conditions, and is consistent with the relative intensities of these eruptions.

#### Cycles of seismicity, magma and gas emission

From 12 to 15 June, discrete periods of intense seismic activity allowed eruptive events to be distinguished. Separate stages in a single eruptive cycle are represented in Fig. 11. Tying together interpretations of  $\text{H}_2\text{O}$  and textural data with observations of the eruptive sequence, we infer the following evolution in conduit conditions during each of the four stages (A–D in Fig. 11) of a single eruptive cycle. During the early part of an explosive phase (A) magmatic volatiles exsolve vigorously, causing expansion and acceleration of the bubbly magma up the conduit. Ground-surface observations include a sharp increase in seismicity followed by growth of a tephra fountain above the vent. Exsolution and subsequent fragmentation occurs under primarily closed-system conditions, since rates of bubble coalescence and volatile diffusion are approximately the same as the rate of magma expulsion. Late in the explosive phase (B), eruption intensity wanes and seis-

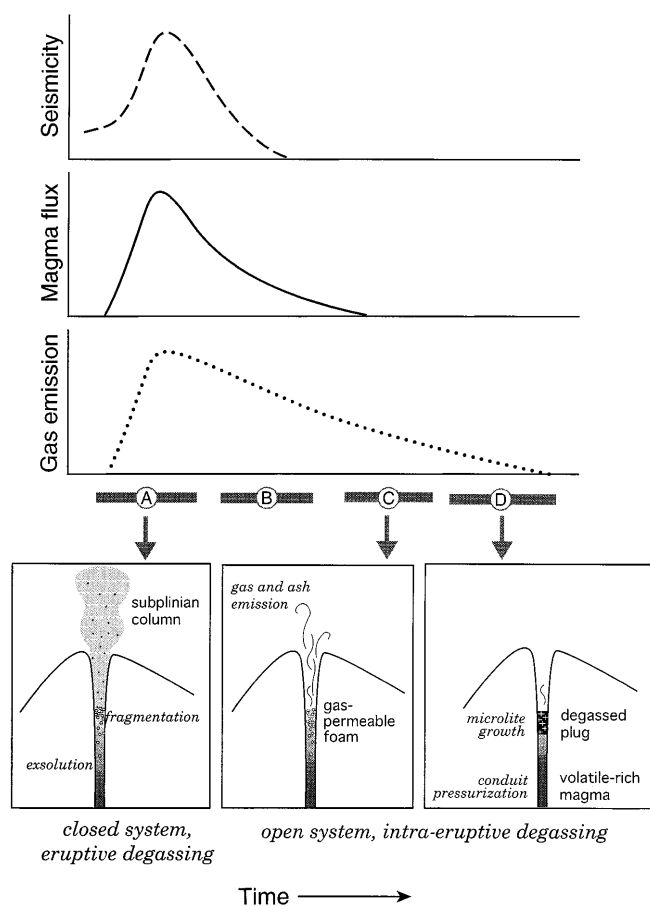


**Fig. 11** Representation of mass eruption rate, gas loss, and seismicity during a single surge-producing event. See text for explanation

micity decreases abruptly. Tephra emission tapers through the final moments of this phase, leaving the conduit filled with an expanded magmatic foam. Degassing switches to dominantly open-system conditions, and the system enters a repose interval (C). Gas and ash emission is still observed at the surface, because the permeable foam structure established during the preceding explosive phase allows exsolved gas to escape. Crystallization of feldspar microlites begins 30–40 min after  $\text{H}_2\text{O}$  exsolution. Efficient gas transfer away from the magma results in a reduction in permeability, eventual foam collapse, and a gradual decline in observed gas emission (D). Degassing and crystallization occur primarily in the upper part of the conduit, resulting in vertical zonation of magma (with respect to volatiles and crystals). A plug of partly degassed, dense, crystallizing magma forms at the top of the magma column and grows downward with time. Because it has experienced less time since gas loss and supersaturation, magma from deeper portions of the plug contains fewer crystals than magma originally near the top of the degassing plug. The lower plug material continues to crystallize in response to the change in phase relations

until the next eruptive event, when it becomes entrained in the explosive expansion of the gas-rich magma below.

The observed distribution of clast densities in the pre-climactic surge deposits (Hoblitt et al. 1996) thus results from variable degassing histories of different parts of the magma column prior to eruption. Gas separation occurring syn-eruptively produced low density pumice, because closed-system conditions prevailed. Conversely, magma that degassed and collapsed in the conduit under open-system conditions (during repose intervals) formed high-density clasts in deposits. The presence of clusters of small vesicles within dense clasts (Fig. 3d) may indicate regions of less degassed liquid surviving from the first degassing stage, fossil pathways of subsurface gas escape, or partial vesiculation resulting from decompression during the next explosive phase. The proposed sequence of exsolution and gas separation with respect to periods of eruption and repose explains critical results of this study: (a) dense clasts are present in all of the deposits; (b) a range in microlite contents is preserved in degassed material, but maximum microlite content ( $\phi_{\max}$ ) varies as a function of repose interval; and (c) dissolved H<sub>2</sub>O contents of dense clasts are similar regardless of eruptive sequence, microlite content, or repose interval duration.

However, a puzzle remains. Since the plug material was still supersaturated with respect to H<sub>2</sub>O at atmospheric pressures at the time of eruption, why did it not vesiculate again during the explosive event that brought it to the surface? One possibility is that 1.4–1.8 wt.% H<sub>2</sub>O is a threshold value necessary for vesiculation at the decompression rates experienced by this magma, i.e., the magma may have simply failed to continue degassing because of the viscosity increase that accompanied extraction of volatiles from the magma. Viscosity estimated using the empirical method of Hess and Dingwell (1996) predicts a liquid viscosity increase of more than two orders of magnitude, from  $10^{4.8}$  to  $10^7$  Pa s, resulting from volatile loss of Pinatubo magma from 5.5 to 1.5 wt.% H<sub>2</sub>O (at 780 °C; Rutherford and Devine 1996). The introduction of 10% solid particles (microlites) imposes an additional two- to six-fold increase in viscosity (Marsh 1981; Pinkerton and Stevenson 1992), resulting in a final viscosity of  $2\text{--}6 \times 10^7$  Pa s.

Dense juvenile dacite produced by the 1980 explosion of a cryptodome at Mount St. Helens also preserves H<sub>2</sub>O contents that exceed equilibrium atmospheric values (Hoblitt and Harmon 1993). Densitometry and volatile analysis suggested that vesiculation was inhibited in magma with less than 0.2–0.4 wt.% H<sub>2</sub>O. Conversely, magma with higher volatile contents freely vesiculated during explosive disruption of the dome. The discrepancy in threshold values inferred for these systems may result from the difference in clast sizes examined from Mount St. Helens (32–64 mm) relative to Mt. Pinatubo (4–16 mm), and the kinetics of quenching during fragmentation. Since small clasts quench faster

than large ones, they may preserve higher dissolved volatile contents.

An alternative explanation is that at least part of the plug solidified by cooling. Although conductive cooling would result in solidification of an insignificant volume over the time scales available between eruptions (Turcotte and Schubert 1982), heat loss due to degassing may be an efficient means of cooling a substantial volume of magma by a few tens of degrees. A temperature gradient within the plug may explain why some dense clasts from each event are microlite poor, independent of H<sub>2</sub>O content or repose interval duration (Fig. 8).

#### Role of degassing in eruptive style

Analysis of another historic pulsatory sequence, the summer 1980 eruptions of Mt. St. Helens (Scandone and Malone 1985), provides a counterpoint to this model. Five explosive events in the months following the cataclysmic 18 May eruption steadily decreased in intensity and volume of magma produced, while the style of eruptive activity progressed from continuous discharge to fitful bursts. Based on estimates of deposit volumes and eruptive time scales, Scandone and Malone (1985) suggested that pulsatory eruptions result from an imbalance in the magma supply rate up the conduit (MSR) and magma discharge rate to the atmosphere (MDR). In their model, the MSR steadily decreased through time as pressure driving eruption waned, but the MDR remained constant because it was controlled by processes of vesiculation and fragmentation. Bursik (1993) generalized this model to suggest that the disparity between MSR and MDR causes pulsatory eruptions. In the case of Mount St. Helens, a gradually decreasing MSR diminished eruptive intensity and frequency following the plinian event. However, at Pinatubo the MSR apparently increased, because the climactic event followed the pulsatory events. Yet, if the MSR increased, why did not the pulses exhibit a crescendo in intensity leading up to the climactic event? Eruptive degassing processes may be part of the answer.

The Pinatubo pattern of increasing eruptive frequency and decreasing intensity culminating in the climactic eruption is mimicked by the phenomenological model of Hoblitt et al. (1996). In this model, eruptions occur when the pressure at the top of the magma column exceeds a confining pressure. Both the magma pressure and the confining pressure change with time: The magma pressure increases continuously with the time elapsed since the volcano reawakened (until the climactic eruption), whereas the confining pressure increases with time elapsed since the start of the repose interval. Although both the magma pressure and the confining pressure increase with time, the rate of magma pressurization increases while the rate of confining pressurization decreases. Thus, the magma pressure eventually exceeds the confining pressure, and an explo-

sive eruption occurs. Eruption-induced depressurization continues until magma pressure becomes too low to sustain an eruption, and a new cycle begins. The climactic eruption starts when the magma pressurization rate exceeds the rate of eruptive depressurization. In their 1996 model, Hoblitt et al. suggested that degassing could be responsible for the changes in the conduit-confining pressure.

Since the parameters governing the phenomenological model were chosen arbitrarily to best mimic the observed behavior, the underlying physical processes responsible for these parameters were not addressed quantitatively. The physical processes of syn-eruptive gas exsolution and intra-eruptive gas escape outlined in the preceding sections could create the changes in confining pressure at the top of the conduit required by the phenomenological model. For example, gas flow through a porous medium may be modeled as a diffusive process so that conduit pressure increases proportionally to  $t^{1/2}$ . Alternatively, the combined effects of gas separation and foam collapse may occur as some other function of time, but preserve the essential characteristics required to generate the appropriate eruptive phenomena (i.e.,  $P$  increases with time,  $dP/dt$  decreases with time). In either case, collapse of devolatilized magma forms a plug that increases confining pressure at the top of the magma column. If the plug thickens during repose intervals, the confining pressure will be proportional to the intra-eruptive (repose) duration. An eruption finally occurs when conduit pressurization due to magma influx exceeds the confining pressure supplied by the thickening degassed plug. As the rate of conduit pressurization continues to increase, the confining pressure will be exceeded after shorter and shorter repose intervals, producing explosive events that diminish in intensity with time, i.e., the observed increase in the frequency of explosive events may be a result of the growing imbalance between rates of conduit pressurization (due to magma influx from below) and development of the confining pressure (due to growth of the degassed plug) resisting eruption. One test of this model would be to examine whether the amount of dense material produced by a given event is proportional to the duration of the repose interval that preceded the event. Unfortunately, volumetrically representative clast density distributions are not available for the pre-climactic events of Mt. Pinatubo.

The results of this study, taken together with the observations and phenomenological model presented by Hoblitt et al. (1996), suggest the following sequence of events for the 1991 pre-climactic activity of Mt. Pinatubo. Gas exsolution during explosive events created high vesicularity, microlite-free pumice characteristic of magma vesiculated under closed-system conditions. Each eruption ended abruptly, leaving partially vesiculated, gas-permeable magma in the upper part of the conduit. This magma experienced microlite growth and open-system gas separation during repose periods. A kinetic delay in crystallization resulted in repose time-

limited crystal growth in response to volatile exsolution. In contrast, rapid exsolution and escape of  $H_2O$  is illustrated by the nearly constant volatile contents of dense clasts, which suggests repeated achievement of an equilibrium at similar conduit pressures. Gas escape eventually caused the inflated foam to collapse, producing a plug of highly viscous material that thickened to the extent allowed by the repose interval duration. Eventually, increasing pressure due to fresh magma injection exceeded the confining pressure in the conduit and initiated another explosive event. The plug of devolatilized, microlite-bearing magma was erupted with the underlying gas-rich magma, and is recognized in surge deposits as vesicle-poor (and often microlite-rich) pyroclasts.

This hypothesis is consistent with the observation that gas emission occurred following each eruptive event, and explains the presence of dense juvenile clasts in pyroclastic deposits as well as the microlite and  $H_2O$  contents of these clasts. The interpretations of crystallization dynamics based on textures are consistent with the proposed timing of volatile loss and crystallization in the Pinatubo eruptive sequence. Rapid, syn-eruptive volatile loss quickly supersaturated the magma with respect to feldspar, but the driving force for crystallization decreased over time as plagioclase crystallization brought the system towards equilibrium.

---

## Conclusion

The following conclusions were reached as a result of this study:

1. Dense tephra produced during each pulse of the pre-climactic eruptive sequence represent fresh, juvenile magma. Textures and volatile contents preserved in these tephra constitute snapshots of the conduit system taken at different times along a devolatilization and crystallization path.
2. Each batch of magma experienced a similar degree of syn- or intra-eruptive volatile loss, indicating that magma in the conduit consistently equilibrated (or was hindered in progress) at pressures of 6.6–16.3 MPa.
3. The pre-climactic dacite compositions are similar to that of the climactic dacite, except that groundmass crystallization in some of the pre-climactic material shifted the  $SiO_2$  content of the liquid from 77.2 to 79.5 wt.%.
4. In view of the short repose interval durations between events, observed groundmass crystallization was probably primarily a response to volatile loss rather than cooling of magma in the conduit.
5. Crystallization occurred during intra-eruptive repose periods. Crystallization was negligible for repose periods < 40 min, rapid during repose intervals of 40–170 min, and moderate during repose intervals > 170 min.

6. High rates of nucleation during the initial stages of crystallization were followed by crystal growth at approximately constant number densities as equilibrium was approached. The crossover from a nucleation- to growth-dominated crystallization regime was accompanied by a change in CSD slopes from steep to shallow, crystal habit from tabular to prismatic, and a reduction in the ratio of surface area to volume.
7. Gas separation from the magma and foam collapse during repose intervals may have generated an impermeable plug at the top of the Pinatubo magma column. This could cause the confining pressure to increase with time, modulating the intensity of subsequent events. This process may also be important in other subplinian eruption sequences.

**Acknowledgements** Images and electron microprobe analyses were collected under the guidance of M. Shaffer at the EPMA facility in the Department of Geological Sciences at the University of Oregon, funded by grants from the W.M. Keck Foundation and the National Science Foundation. We thank J. Pallister for samples of Pinatubo andesite and climactic dacite. Reviews by C. Gardner, J. Lowenstern, M. Higgins, and M. Rutherford improved the manuscript and are greatly appreciated. This study was supported by grants to K. Cashman (NSF EAR-9418008 and EAR-9614753) and to E. Stolper (NSF OCE-9416747 and DOE DEFG03-85ER13445).

## Appendices

### Appendix A: Microprobe glass analysis

The high microlite content of most clasts prevented microprobe analysis using ideal operating conditions (low beam current, large spot size, and long count times) for the analysis of hydrous glasses in which alkali loss is likely to be problematic. Consequently, all clasts were first analyzed using a 1- to 10- $\mu\text{m}$  diameter and 10-nA beam at 15 keV. Glass standards were used for all oxides except  $\text{TiO}_2$ ,  $\text{Na}_2\text{O}$ , Cl, and  $\text{K}_2\text{O}$ , for which rutile, albite, scapolite, and orthoclase mineral standards were employed, respectively. Then the  $\text{Na}_2\text{O}$ ,  $\text{K}_2\text{O}$ ,  $\text{SiO}_2$ , and  $\text{Al}_2\text{O}_3$  contents of the glasses from three microlite-free clasts were re-analyzed using conditions previously observed to minimize alkali loss in hydrous glasses: 20-nA beam current, 20- $\mu\text{m}$  spot diameter, and 30-s counting time (Morgan and London 1996). Furthermore, the instrument standardization was verified periodically during analysis using these experimental conditions. In all three clasts, the average  $\text{Na}_2\text{O}$  values from the re-analyzed glasses were  $\approx 10\%$  greater than the original sample averages, indicating that significant Na loss occurred as a result of the small spot size. The other oxides differed by  $\approx 1\%$  but tended to increase in the re-analysis. Since all dense, pre-climactic dacite clasts analyzed by FTIR contain comparable  $\text{H}_2\text{O}$  contents and are similar in composition, the magnitude of Na loss resulting from the original operating conditions was pre-

sumed similar. Therefore, probe data for pre-climactic dacite reported in Table 5 were adjusted by multiplicative factors obtained from the re-analysis ( $\text{SiO}_2$ : 1.007;  $\text{Al}_2\text{O}_3$ : 1.006;  $\text{K}_2\text{O}$ : 1.014; and  $\text{Na}_2\text{O}$ : 1.098). Analyses of andesite and climactic material were not adjusted because their compositions and/or  $\text{H}_2\text{O}$  contents differ from the dense, microlite-free dacite used in the broad spot analysis mode.

### Appendix B: Hydration of Pinatubo glasses

Clast density appears to correlate inversely with  $\text{H}_2\text{O}_{\text{Total}}$  (Fig. B1). This trend may reflect post-eruptive hydration of glasses, which would have been facilitated by the greater surface areas of vesicle-bearing clasts. However, the correlation is very weak and speciation data were used to determine whether individual analyses included hydrated areas.

All analyses are plotted in Fig. B2 along with experimentally determined isotherms (Stolper 1989; Zhang et al. 1995) and data from Mono Craters obsidians having a similar range in  $\text{H}_2\text{O}_{\text{T}}$  (Newman et al. 1988). We know of no established means to determine whether analyses reflect hydration from external  $\text{H}_2\text{O}$  sources. We excluded from sample averages analyses falling away from the Mono trend and well below the  $400^\circ$  isotherm. Interestingly, analyses suspected to reflect post-eruptive hydration based on speciation data span a range in  $\text{H}_2\text{O}_{\text{T}}$  identical to that of areas considered pristine. Furthermore, inclusion of all analyses still represents  $\text{H}_2\text{O}$  loss of at least 3 wt.% with respect to the original volatile content determined for the Pinatubo liquid (5.5–6.4 wt.%  $\text{H}_2\text{O}$ ; Rutherford and Devine 1996). We therefore conclude that post-eruptive hydration has not significantly affected our results.

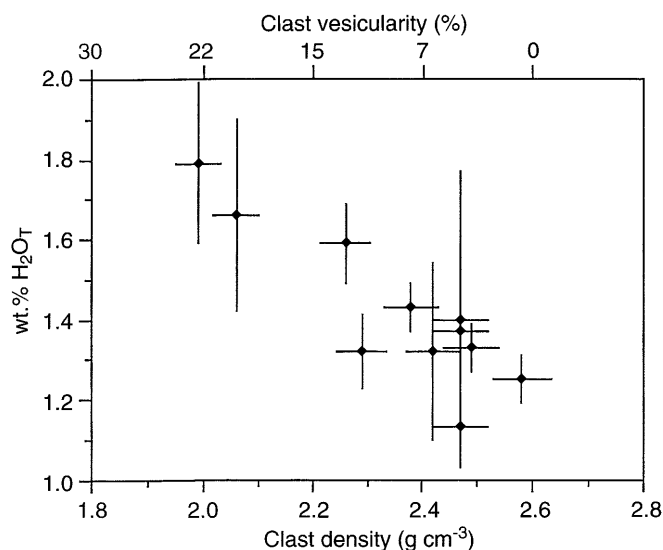


**Fig. B.1** Clast density and  $\text{H}_2\text{O}_{\text{T}}$ . Data are clast averages. Error bars in  $\text{H}_2\text{O}$  contents are  $\pm 1$  s from clast averages. Error bars in density data are 2%

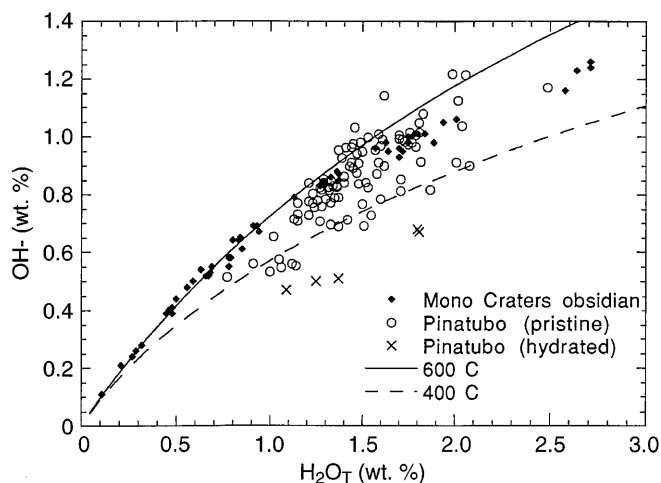


**Fig. B.2**  $H_2O_T$  and weight percent  $OH^-$  for Pinatubo and Mono Craters samples. Isotherms represent experimental data compiled in Newman et al. (1988).  $X$  represents analyses suspected to represent hydrated areas and were not included in clast averages (Table 3);  $O$  represents analyses of pristine areas. The  $OH^-$  contents of Pinatubo values are similar to those of Mono Craters, CA (diamonds) over the shared range in  $H_2O_T$ , and fall between the 400 and 600 °C isotherms

The equilibration temperature indicated by the relative abundance of molecular  $H_2O$  and  $OH^-$  groups is 400–600 °C. Because the rate of equilibration is limited by the kinetics of the speciation reaction



(Stolper 1982), the recorded temperature is a function of both the total  $H_2O_T$  content and the time available to respond to dropping temperature. Since the original magmatic temperature was determined to be 780 °C (Rutherford and Devine 1996) on the basis of phase equilibria, it is likely that the  $H_2O_T$  speciation temperature simply records the lowest temperature at which speciation equilibration could keep pace with cooling for these  $H_2O_T$  values. The median cooling rate (determined using the geospeedometry calculation of Zhang et al. 1997) of  $1.6^\circ\text{C s}^{-1}$  for all clasts is also similar to that of pyroclastic glass fragments from Mono Craters,  $\sim 3^\circ\text{C s}^{-1}$  (Zhang et al. 1995).

### Appendix C: Textural characterization

Measurements of  $N_A$ ,  $\phi$ , and crystal shape required different treatments of edge-intersecting crystals. As suggested by Russ (1986), microlites touching only two of the four image edges were counted for use in number density ( $N_A$ ) calculations. Microlite crystallinity,  $\phi$ , was obtained from point counts of printed images. Because total microlite area is required for  $\phi$  measurements, all edge-intersecting crystals were included in the point counts. For crystal size and shape determinations, only those crystals completely contained within the image were outlined. The minimum (breadth) and maximum

(length) dimensions of each crystal were measured using NIH Image.

### Crystallinity, number density, and mean size

Crystal number density (number of crystals per square millimeter) and  $\phi$  were calculated on a phenocryst- and vesicle-free basis, so that the relevant area in each backscattered electron (BSE) image consists of only glass and microlites. We refer to this as the “reference area,” obtained by subtracting phenocryst and vesicle areas from the total image area (in this case,  $2603.54 \mu\text{m}^2$ ). Measurements were weighted by image reference area when combined to determine average values for each clast. Microlite number densities were obtained by manual identification to obtain a per area (per square millimeter) count. Image crystallinities were obtained from simple point counts using a transparent grid with 1620 intersections. The average microlite area was obtained by dividing the total crystal area by the number of crystals. Mean microlite size ( $s_n$ ) is expressed as the square root of the average microlite area, and may be computed directly from  $N_A$  and  $\phi$  as

$$s_n = (\phi/N_A)^{0.5} \quad (4)$$

As a confirmation of image analysis methods for determining the feldspar microlite content, the mode of microlites and glass in the groundmass of several clasts was computed from the glass and feldspar compositions using multiple linear regression techniques. We assumed that the composition of a virtually microlite-free glass from clast P801 (Table 5) represented the “bulk” composition of the rhyolite liquid prior to microlite crystallization. Feldspars were partitioned between two end-member compositions represented by the Pinatubo microlites, and the mode of feldspars and glass in each clast were computed using  $SiO_2$ ,  $Al_2O_3$ ,  $CaO$ ,  $Na_2O$ , and  $K_2O$  contents of the phases. The results, converted to volume percent, are plotted against the mode obtained using image analysis in Fig. C1. The good correspondence of these independent methods provides verification of the image processing method for determining microlite content.

### Microlite shape

Shapes of crystals growing in melts are controlled by the kinetics of crystallization (specifically, the relative growth rates of individual crystal faces) and may provide information about the degree of undercooling experienced by sequential batches of magma en route to the surface (Lofgren 1980). Higgins (1994) showed that a statistical analysis of the two-dimensional intersections of a random plane with a single crystal can be used to obtain its true (three-dimensional) aspect ratio. Measurements necessary for the analysis are shortest

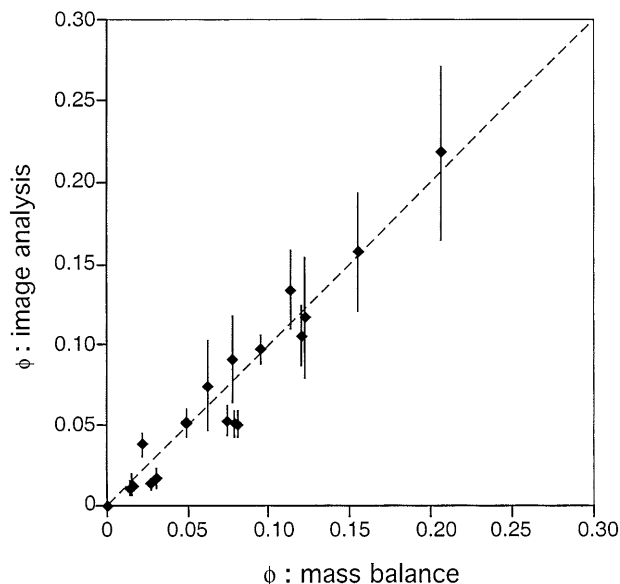


**Fig. C.1** Verification of image analysis technique for obtaining microlite volume fraction. Vertical axis shows  $\phi$  values obtained from image analysis; horizontal axis is  $\phi$  calculated using original matrix glass and end-member feldspar compositions. For reference, diagonal line is 1:1

(breadth,  $b$ ) and longest (length,  $l$ ) dimensions of the crystal in thin section (two dimensions). For randomly oriented slices through the crystal, the modal value of the aspect ratio ( $b/l$ ) in a two-dimensional slice is equal to the ratio of the short to intermediate dimension in three dimensions. The ratio of the true intermediate to longest dimension is proportional to the skewness of the aspect ratio distribution; positive skewness indicates tablet-shaped crystals, whereas negative skewness is correlated with prismatic shapes. This treatment is also valid for a population of crystals of varying size if all of the crystals are the same shape. Using measurements of microlite breadth and length, and applying the techniques from Higgins (1994), the three-dimensional axis ratios ( $S$ =short;  $I$ =intermediate/short;  $L$ =long/short) were computed. The average shortest, intermediate, and longest dimensions ( $a$ ,  $b$ , and  $c$ , respectively) of microlites may then be calculated by combining the axial ratios ( $S$ ,  $I$ , and  $L$ ) with the average crystal linear size,  $s_n$ , obtained from  $N_A$  and  $\phi$  measurements:

$$a = s_n (I^{-1/2}) \quad (5)$$

$$b = s_n (I^{1/2}) \quad (6)$$

$$c = s_n (L/I) \quad (7)$$

#### Microlite crystal size distributions

Crystal size distributions (CSDs) can provide information about the rates of nucleation and growth of crystal populations if time scales of crystallization are known. Determination of CSDs from thin section measure-

ments requires both a choice of linear characteristic size,  $\mathcal{L}$ , and conversion of measurements from a per-area to per-volume basis. Errors in the conversion include the cut effect (resulting from sectioning through edges and corners), the intersection problem (in which small crystals are intersected less frequently than large crystals) and distortions introduced by the non-spherical habit of most crystals (Ripley 1981; Russ 1986; Underwood 1970). The simplest way of accounting for the first two problems is to use the relationship

$$N_V = N_A/d \quad (8)$$

for each bin size,  $d$  (Underwood 1970). However, this method does not correct for varying crystal shape. Following the method of Peterson (1996), which addresses the problem of shape, and employing the shape characterization techniques described previously from Higgins (1994), we converted breadth ( $b$ ) measurements into true crystal lengths ( $\mathcal{L}$ ), so that

$$\mathcal{L} = b * L, \quad (9)$$

and determined the CSDs for seven clasts (Fig. 7). The complete CSDs with and without application of the Peterson shape correction are shown for two clasts in Fig. C2. Note that the correction results in a dramatic reduction in the scatter of the data, but does not cause an appreciable shift in  $n^\circ$  or slope compared with the uncorrected CSDs (where  $N_V$  is simply equal to  $N_A/d$ ). The data define a linear trend over most of the range in size measured, with values falling off below 0.002 mm, perhaps because of a lower size detection limit with BSE imaging. The remainder of each distribution was fit to a linear function in order to determine the average crystal size and rates of nucleation and growth. As described by Randolph and Larson (1971) and Marsh (1988, 1998), and as applied by Cashman (1992, 1993), Higgins (1996a), Waters and Boudreau (1996), and Wilhelm and Woerner (1996), among others, the slope of the curve relating frequency to linear size is equal to the average crystal size

$$\text{slope} = -1/(\text{average } \mathcal{L}) = -1/G \tau, \quad (10)$$

where  $G$  is the average linear growth rate and  $\tau$  is the duration of crystal growth. Therefore, if  $\tau$  is known, the average linear crystal growth rate can be determined. The nucleation rate,  $J$ , is the product of the average growth rate and the number density of crystals having zero size (y-intercept value,  $n^\circ$ ):

$$J = n^\circ G. \quad (11)$$

As described by Cashman (1992), the slope and intercept may be used to determine the crystal area number density, volumetric number density, and volume fraction:

$$N_A = n^\circ (-1/G\tau)^2 \quad (12)$$

$$N_V = n^\circ (-1/G\tau) \quad (13)$$

$$\phi = 6 n^\circ (-1/G\tau) k, \quad (14)$$

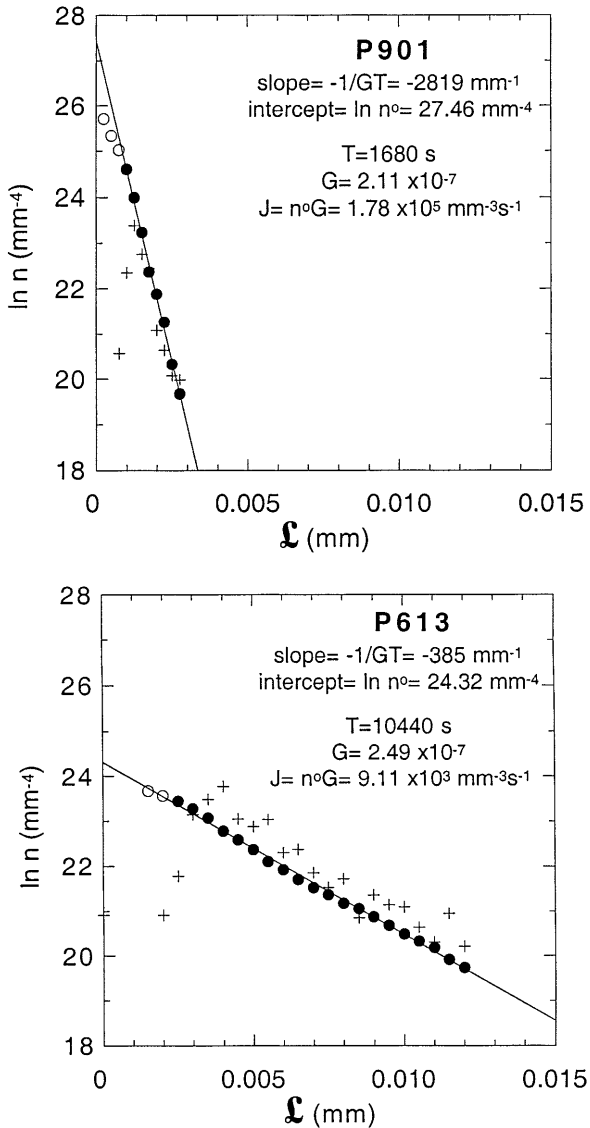


**Fig. C.2** Complete CSDs for two end-member microlite populations. + symbols represent data uncorrected for microlite shape (i.e.,  $N_V N_A/d$ ). Circles represent the same crystal length measurements corrected for shape using the methods described by Peterson (1996). Open symbols were not included in linear fits to the data. Average microlite growth rate ( $G$ ) and nucleation rate ( $J$ ) are calculated for clasts P901 and P613 using the slopes and intercepts of the CSDs and assuming that the repose durations ( $\tau$ ) represent the time scales over which crystallization occurred (see Table 1)

where we used  $k = (I) (L^{-2})$ . The values of number density and total volume percent crystals determined from CSDs may be compared with the results from direct image analysis (Table 7). To a first-order approximation, the two methods yield similar results. For example, the average crystal sizes determined from the CSDs of all clasts were within a factor of two of values of  $s_n$  derived from measurements of  $N_A$  and  $\phi$  using image analysis. However, the area number densities obtained from CSD parameters are consistently high relative to

the image analysis measurements by factors of 1.5–5. The CSD-derived volume fractions are higher by factors of 1.5–4 (one value is lower by a factor of 0.67). Given the satisfactory agreement of compositional (mass balance) and image analysis methods for obtaining crystallinity (Fig. C1), the values obtained from the CSD analysis are called into question. One of several sources of error embedded in the calculations may be responsible for discrepancy in results. The difference in  $N_A$  values between the methods is probably a consequence of the length scale chosen for the construction of CSDs. The  $\mathcal{L}$  values determined using Eq. (9) are greater than the length scale represented from the image analysis method,  $s_n$  (Eq. 4), and therefore boost the calculation of  $N_A$  using Eq. (12). The assessment of crystal shape assumes that all crystals are the same shape, or that a single shape is a good approximation for the range of shapes present. Given that the average crystal shape is shown to vary significantly among clasts, there is certainly some variation *within* each clast. The magnitude of the error induced by this assumption is difficult to assess, since there is no way to compute a three-dimensional shape distribution from two-dimensional measurements. However, given that shape varies with size, and that the range of crystal sizes in any single clast is limited, the range in shapes is probably negligible as well.

Error is also introduced in the calculation of correction factors ( $S$ ,  $\gamma$ ; e.g., Peterson 1996), which is predicated on the assumption of uniaxial symmetry. Some crystal habits were far from uniaxial (e.g., P701:  $\sim 1:3:6$ ), having habits intermediate between tablet and prism. The substitution of the best-fit uniaxial shape in the calculation of correction factors is clearly less appropriate for these samples. Finally, moment statistics used in the calculation of nucleation rate and number density are sensitive to the extrapolated population densities,  $n$ , at  $\mathcal{L}=0$  ( $n^0$ , the y-intercept). If the crystals are *not* exponentially distributed over the entire range of sizes, the values of these parameters will be under- or overestimated. For example, if the downturn in population density at the smallest size classes (see Fig. C2) is real, not a sampling artifact, the number density obtained using the extrapolated intercept is an overestimate. Again, this assumption is difficult to assess, since the smallest-sized crystals can be difficult to recognize and measure given the limits of resolution using electron-beam imaging techniques.

Similarly, the extrapolation of the curve to infinitely large sizes may boost the volume percent crystals as estimated using CSD theory. Given that the crystals in question are microlites rather than phenocrysts, the supposition that large crystals exist, even in very small numbers, is probably not valid. In order to test the error dependence on integration limits, we computed volume percent using the maximum observed size rather than infinity as the upper limit. The recalculated values of volume percent are closer to the image analysis values in six of the seven clasts (Table 7).

## References

- Bernard A, Knittel U, Weber B, Weis D, Albrecht A, Hattori K, Klein J, Oles D (1996) Petrology and geochemistry of the 1991 eruption products of Mount Pinatubo. In: Newhall CG, Punongbayan RS (eds) Fire and mud: eruptions and lahars of Mount Pinatubo, Philippines. University of Washington Press, Seattle, pp 767–797
- Brandeis G, Jaupart C (1987) The kinetics of nucleation and crystal growth and scaling laws for magmatic crystallization. *Contrib Mineral Petrol* 96:24–34
- Burnham CW, Davis NF (1974) The role of H<sub>2</sub>O in silicate melts: II. Thermodynamic and phase relations in the system NaAl-Si<sub>2</sub>O<sub>8</sub>-H<sub>2</sub>O to 10 kilobars, 700 C–1100 C. *Am J Sci* 274:902–940
- Bursik M (1993) Subplinian eruption mechanisms inferred from volatile and clast dispersal data. *J Volcanol Geotherm Res* 57:57–70
- Cashman KV (1992) Groundmass crystallization of Mount St. Helens dacite, 1980–1986: a tool for interpreting shallow magmatic processes. *Contrib Mineral Petrol* 109:431–449
- Cashman KV (1993) Relationship between crystallization and cooling rate—insight from textural studies of dikes. *Contrib Mineral Petrol* 113:126–142
- Cashman KV, Mangan MT (1994) Physical aspects of magmatic degassing II: constraints on vesiculation processes from textural studies of eruptive products. In: Carroll MR, Holloway JR (eds) Volatiles in magmas. Mineralogical Society of America, Washington, DC, pp 447–478
- Dobson PF, Epstein S, Stolper EM (1989) Hydrogen isotope fractionation between coexisting vapor and silicate glasses and melts at low pressure. *Geochim Cosmochim Acta* 53:2723–2730
- Eichelberger JC (1989) Are extrusive rhyolites produced from permeable foam eruptions? A reply. *Bull Volcanol* 51:72–75
- Eichelberger JC, Carrigan CR, Westrich HR, Price RH (1986) Non-explosive silicic volcanism. *Nature* 323:598–602
- Gardner CA, Cashman KV, Neal CA (1998) Tephra-fall deposits from the 1992 eruption of Crater Peak, Alaska: implications of clast textures for eruptive processes. *Bull Volcanol* 59:537–555
- Geschwind C, Rutherford MJ (1995) Crystallization of microlites during magma ascent: the fluid mechanics of recent eruptions at Mount St. Helens. *Bull Volcanol* 57:356–370
- Hammer JE, Cashman KV (1995) Insights into the eruptive mechanism of the 1991 eruptions of Mount Pinatubo, Philippines, provided by textural analysis of pre-climactic eruptive material. *EOS* 76:680
- Hammer JE, Cashman KV, Voight B Magmatic processes revealed by textural and compositional trends in Merapi dome lavas. *J Volcanol Geotherm Res* (in press)
- Heiken G, Wohletz K (1987) Tephra deposits associated with silicic domes and lava flows. *Geol Soc Am Spec Pap* 212:55–76
- Hess K-U, Dingwell DB (1996) Viscosities of hydrous leucogranitic melts: a non-Arrhenian model. *Am Mineral* 81:1297–1300
- Higgins MD (1994) Numerical modeling of crystal shapes in thin sections: estimation of crystal habit and true size. *Am Mineral* 79:113–119
- Higgins MD (1996a) Crystal size distributions and other quantitative textural measurements in lavas and tuff from Egmont Volcano (Mt. Taranaki), New Zealand. *Bull Volcanol* 58:194–204
- Higgins MD (1996b) Magma dynamics beneath Kameni Volcano, Greece, as revealed by crystal size and shape measurements. *J Volcanol Geotherm Res* 70:37–48
- Hildreth W, Drake RE (1992) Volcan Quizapu, Chilean Andes. *Bull Volcanol* 54:93–125
- Hoblitt RP, Harmon RS (1993) Bimodal density distribution of cryptodome dacite from the 1980 eruption of Mount St. Helens, Washington. *Bull Volcanol* 55:421–437
- Hoblitt RP, Wolfe EW, Scott WE, Couchman MR, Pallister JS, Javier D (1996) The preclimactic eruptions of Mount Pinatubo, June 1991. In: Newhall CG, Punongbayan RS (eds) Fire and mud: eruptions and lahars of Mount Pinatubo, Philippines. University of Washington Press, Seattle, pp 457–512
- Houghton BF, Wilson CJN (1989) A vesicularity index for pyroclastic deposits. *Bull Volcanol* 51:451–462
- Kirkpatrick RJ (1981) Kinetics of crystallization of igneous rocks. In: Lasaga A, Kirkpatrick R (eds) Kinetics of geochemical processes. Mineralogical Society of America, Washington, DC, pp 321–397
- Klug C, Cashman KV (1994) Vesiculation of May 18, 1980, Mount St. Helens magma. *Geology* 22:468–472
- Klug C, Cashman KV (1996) Permeability development in vesiculating magmas: implications for fragmentation. *Bull Volcanol* 58:87–100
- Lange RL, Carmichael ISE (1990) Thermodynamic properties of silicate liquids with emphasis on density, thermal expansion and compressibility. In: Nicholls J, Russell JK (eds) Modern methods of igneous petrology; understanding magmatic processes. Mineralogical Society of America, Washington, DC, pp 25–64
- Lasaga AC (1981) Implications of a concentration-dependent growth rate on the boundary layer crystal-melt model. *Earth Planet Sci Lett* 56
- Lofgren GE (1980) Experimental studies on the dynamic crystallization of silicate melts. In: Hargraves R (ed) Physics of magmatic processes. Princeton University Press, Princeton, New Jersey, pp 487–551
- Marsh BD (1981) On the crystallinity, probability of occurrence, and rheology of lava and magmas. *Contrib Mineral Petrol* 78:85–98
- Marsh BD (1988) Crystal size distributions (CSD) in rocks and the kinetics and dynamics of crystallization. I. Theory. *Contrib Mineral Petrol* 99:277–291
- Marsh BD (1998) On the interpretation of crystal size distributions in magmatic systems. *J Petrol* 39:553–599
- Mastrolorenzo G, Munno R, Rolandi G (1993) Vesuvius 1906; a case study of a paroxysmal eruption and its relation to eruption cycles. *J Volcanol Geotherm Res* 58:217–237
- Mellors RA, Sparks RSJ (1991) Spatter-rich pyroclastic flow deposits on Santorini, Greece. *Bull Volcanol* 53:327–342
- Morgan GBV, London D (1996) Optimizing the electron microprobe of hydrous alkali aluminosilicate glasses. *Am Mineral* 81:1176–1185
- Muncill G, Lasaga A (1988) Crystal-growth kinetics of plagioclase in igneous systems: isothermal H<sub>2</sub>O-saturated experiments and extension of a growth model to complex silicate melts. *Am Mineral* 73:982–992
- Nakada S, Motomura Y (1995) Manner of magma ascent at Unzen Volcano (Japan). *Geophys Res Lett* 22:567–570
- Newman S, Epstein S, Stolper EM (1988) Water, carbon dioxide, and hydrogen isotopes in glasses from the ca. 1340 A.D. eruption of the Mono Craters, California: constraints on degassing phenomena and initial volatile content. *J Volcanol Geotherm Res* 35:75–96
- Newman S, Stolper EM, Epstein S (1986) Measurement of water in rhyolitic glasses: calibration of an infrared spectroscopic technique. *Am Mineral* 71:1527–1541
- Pallister JS, Hoblitt RP, Meeker GP, Knight RJ, Siems DF (1996) Magma mixing at Mount Pinatubo: petrographic and chemical evidence from the 1991 deposits. In: Newhall CG, Punongbayan RS (eds) Fire and mud: eruptions and lahars of Mount Pinatubo, Philippines. University of Washington Press, Seattle, pp 687–732
- Peterson TD (1996) A refined technique for measuring crystal size distributions in thin section. *Contrib Mineral Petrol* 124:395–405
- Pinkerton H, Stevenson RJ (1992) Methods of determining the rheological properties of magmas at sub-liquidus temperatures. *J Volcanol Geotherm Res* 53:47–66

- Randolph AD, Larson MA (1971) Theory of particulate processes. Academic Press, New York
- Ripley BD (1981) Spatial statistics. Wiley, New York
- Rogers JP (1996) Analysis of tephra components from Rock Mesa, South Sister Volcano, Oregon: implications for evolution of the explosive phase. Masters Thesis, University of Oregon, Eugene, Oregon, 85 pp
- Russ JC (1986) Practical stereology. Plenum, New York
- Rutherford MJ, Devine JD (1996) Preeruption pressure-temperature conditions and volatiles in the 1991 dacitic magma of Mount Pinatubo. In: Newhall C, Punongbayan R (eds) Fire and mud: eruptions and lahars of Mount Pinatubo, Philippines. University of Washington Press, Seattle, pp 751-766
- Rutherford MJ, Hill PM (1993) Magma ascent rates from amphibole breakdown: experiments and the 1980-1986 Mount St. Helens eruptions. *J Geophys Res* 98:19667-19685
- Scandone R, Malone SD (1985) Magma supply, magma discharge and readjustment of the feeding system of Mount St. Helens during 1980. *J Volcanol Geotherm Res* 23:239-262
- Stolper E (1982) Water in silicate glasses: an infrared spectroscopic study. *Contrib Mineral Petrol* 81:1-17
- Stolper E (1989) Temperature dependence of the speciation of water in rhyolitic melts and glasses. *Am Mineral* 74:1247-1257
- Swanson SE (1977) Relation of nucleation and crystal-growth rate to the development of granitic textures. *Am Mineral* 62:966-978
- Swanson SE, Naney MT, R WH, Eichelberger JC (1989) Crystallization history of Obsidian dome, Inyo domes, California. *Bull Volcanol* 51:161-176
- Turcotte DL, Schubert G (1982) Geodynamics: applications of continuum physics to geological problems. Wiley, New York
- Underwood EE (1970) Quantitative stereology. Addison-Wesley, Reading, Mass.
- Waters C, Boudreau AE (1996) A reevaluation of crystal-size distributions in chromite cumulates. *Am Mineral* 81:1452-1459
- Westrich HR, Stockman HW, Eichelberger JC (1988) Degassing of rhyolitic magma during ascent and emplacement. *J Geophys Res* 93:6503-6511
- Wilhelm S, Woerner G (1996) Crystal size distributions in Jurassic Ferrar flows and sills (Victoria Land, Antarctica): evidence for processes of cooling, nucleation, and crystallisation. *Contrib Mineral Petrol* 125:1-15
- Wolf KJ, Eichelberger JC (1997) Syneruptive mixing, degassing, and crystallization at Redoubt Volcano, eruption of December 1989 to May 1990. *J Volcanol Geotherm Res* 75:19-37
- Zhang Y, Jenkins J, Zhengjiu X (1997) Kinetics of the reaction  $H_2O + O \leftrightarrow 2OH$  in rhyolitic glasses upon cooling: geospeedometry and comparison with glass transition. *Geochim Cosmochim Acta* 61:2167-2173
- Zhang Y, Stolper EM, Ihinger PD (1995) Kinetics of reaction  $H_2O + O = 2OH$  in rhyolitic glasses: preliminary results. *Am Mineral* 80:593-612